INTERNATIONAL JOURNAL FOR NUMERICAL METHODS IN FLUIDS
Int. J. Numer. Meth. Fluids 2005; **48**:869–908
Published online 15 March 2005 in Wiley InterScience (www.interscience.wiley.com). DOI: 10.1002/fld.965

Time-accurate intermediate boundary conditions for large eddy simulations based on projection methods

F. M. Denaro*,†

Dipartimento di Ingegneria Aerospaziale e Meccanica, Seconda Universita' degli Studi di Napoli, Italy

SUMMARY

Projection methods are among the most adopted procedures for solving the Navier–Stokes equations system for incompressible flows. In order to simplify the numerical procedures, the pressure–velocity decoupling is often obtained by adopting a fractional time-step method. In a specific formulation, suitable for the incompressible flows equations, it is based on a formal decomposition of the momentum equation, which is related to the Helmholtz–Hodge Decomposition theorem of a vector field in a finite domain. Owing to the continuity constraint also in large eddy simulation of turbulence, as happens for laminar solutions, the filtered pressure characterizes itself only as a Lagrange multiplier, not a thermodynamic state variable. The paper illustrates the implications of adopting such procedures when the decoupling is performed onto the filtered equations system. This task is particularly complicated by the discretization of the time integral of the sub-grid scale tensor. A new proposal for developing time-accurate and congruent intermediate boundary conditions is addressed. Several tests for periodic and non-periodic channel flows are presented. This study follows and completes the previous ones reported in (*Int. J. Numer. Methods Fluids* 2003; **42**, **43**). Copyright © 2005 John Wiley & Sons, Ltd.

KEY WORDS: fractional time-step method; large eddy simulation; pressure-free projection method; intermediate boundary conditions

1. INTRODUCTION

The extension of numerical methods that are commonly used for solving the Navier–Stokes (NS) equations for laminar, isothermal, incompressible flows, to a form that is also suitable for the large eddy simulation (LES) of turbulent flows is only apparently a straightforward task.

As it is known, differently from direct numerical simulation (DNS), LES is based on a formal separation between large (resolved) and small (unresolved) flow scale contributions, obtained from the application of a filtering procedure on both continuity and momentum

*Correspondence to: F. M. Denaro, Dipartimento di Ingegneria Aerospaziale e Meccanica, Real Casa dell' Annunziata, Via Roma 29, 81031, Aversa (CE), Italy.
†E-mail: denaro@unina.it

Received 12 May 2004
Revised 5 January 2005
Accepted 31 January 2005

equations (e.g. see Reference [1]). Thus, the unresolved sub-grid scale (SGS) tensor must be modelled in terms of the resolved field by means of some suitable functional relation. Such additional SGS tensor is a function of space and time and has to be properly discretized, congruently with the other terms in the momentum equation.

An important concept is that the filtered pressure characterizes itself only as a Lagrange multiplier used to satisfy the continuity constraint, not a thermodynamic state variable, exactly as it happens for the DNS. Therefore, heavy computational procedures would be needed also in LES for solving the resultant Stokes-like system. In order to simplify such procedures, a velocity–pressure de-coupling is often introduced, allowing us to solve separately the parabolic–elliptic equations. A fractional time-step (FTS) method, expressed in a specific formulation suitable for incompressible flows, is based on a formal decomposition of the momentum equation. This idea is strictly related to the Helmholtz–Hodge Decomposition (HHD) theorem of a vector field in a finite domain (e.g. see References [2–6]) from which the name *projection methods* comes too.

The FTS method provides the solution of the NS equations in certain separated steps. The first one is simply based on the solution of the time-discretized momentum equation. One speaks of *incremental-pressure projection methods* if a provisional pressure gradient is used, otherwise of *pressure-free projection* (PFP) *methods*. This prediction equation must be associated to a suitable set of *intermediate boundary conditions* for parabolic-type equations. Its solution provides a non-solenoidal velocity vector field, say $\mathbf{v}^*$, which must be afterwards projected onto the space of divergence-free vector functions. Hence, the second step consists in solving the elliptic Poisson equation for an auxiliary gradient field, say $\nabla\phi$, associated to proper closure conditions, and is needed to enforce continuity. According to the HHD, the last step is the correction of $\mathbf{v}^*$ by means of the computed gradient field ensuring a final velocity which satisfies the continuity constraint.

In the first step of the FTS methodology, a semi-implicit, multi-step, second-order time-accurate discretization, as the Adams–Bashforth/Crank–Nicolson (in the following simply indicated as AB/CN) scheme, is often adopted, e.g. see References [7, 8]. In this method the equation for $\mathbf{v}^*$ is obtained by performing first the AB/CN integration of the momentum equation and, thereafter, by disregarding the time integral of the pressure term. For DNS it is usual to cast the non-linear convective terms within the AB integration and the linear molecular diffusive ones within the CN. When approaching the LES equations, one has also to discretize the time integral of the SGS tensor, by choosing if including it into either the AB or the CN discretization. Depending on such choice, the nature of the resulting system is either linear or non-linear, and the resulting provisional fields $\mathbf{v}^*$ gets different meanings. Therefore, intermediate boundary conditions assigned during the first step must account for the real meaning of the provisional vector field that depends on both filtering and turbulence modelling.

Following the HHD theorem, the boundary conditions for the second step (i.e. the Poisson equation) prescribe that the normal component of the boundary value for $\mathbf{v}^*$ is equal to the normal component of $\nabla\phi$ plus that one of the exact velocity. Therefore, the Neumann boundary conditions for the auxiliary gradient field set the solution to satisfy exactly the mass-flow boundary condition, while ensuring continuity. The solution of the Poisson problem cannot ensure that also the tangential component turns to be satisfied, at least at the same second-order accuracy resulting in the interior. This is due to the potential character of the auxiliary variable ϕ. As a consequence of the HHD theorem, the mathematical problem is

well posed by specifying only one boundary condition,[‡] the others remaining affected by the approximate values of $\mathbf{v}^*$ already prescribed in the first step. Therefore, the FTS method never allows us to exactly satisfy both the normal and the tangential velocity assignments on the boundaries. A simple and generally used remedy is to disregard the tangential components that are obtained in the third step and reset them to their known values on the boundary, at the end of each time-step. Nevertheless, it was clearly shown that such strategy is poorly accurate and can reduce the smoothness of the velocity field [8, 9]. Hence, accurate intermediate boundary conditions can be deduced provided that the correct relations between the real filtered velocity, pressure gradient and the auxiliary fields are adopted. Several proposals for prescribing higher order intermediate boundary conditions can be found in literature, e.g. see References [7–11].

Projection methods are now massively used in LES and the PFP method is routinely implemented in several LES codes but, to date, no complete study has been published to determine what time scales are well resolved and how they influence the solution. To the best of the authors' knowledge, this issue has not been deeply analysed in the literature. However, some results (e.g. References [12, 13]) seem to indicate that time filtering effects can become large even for moderate time-steps.

In the present paper, the intermediate boundary conditions necessary only for the PFP method are considered, incremental projection methods being not examined. It is worthwhile addressing several well assessed results concerning the accuracy analysis of the PFP methods for laminar flows in References [8, 9, 14–19] while the well known Van Kan second-order method [20] belongs to the class of the pressure correction ones.

The main goal of the present paper consists in providing an insight into the theoretical analysis of the PFP method used for the LES while proposing a new procedure for improving the accuracy of the intermediate boundary conditions. For reaching this goal and continuing in the spirit of the continuous formulation proposed in papers [10, 11], the field $\mathbf{v}^*$ is supposed to be a regular solution of a suitable partial differential equation. Thus, it is highlighted why it is not recommended to adopt the CN integration of the SGS model while a boundary condition expression, fulfilling the goal of congruence and accomplishing the closure of the problem with fully accuracy, will be proposed for the AB integration.

Some theoretical conclusions, derived for the unfiltered NS equations, can be found in References [10, 11]. Here, after the analysis for the LES equations, a section illustrates the numerical solutions obtained for the classical test-case of the turbulent periodic channel flow with steady and unsteady forcing pressure. The results are obtained in both DNS and LES formulations and show some statistical quantities, like the spectra of the stresses on the walls and the root mean square (rms) quantities of the velocity fluctuations, compared for both the classical intermediate boundary condition and the present new proposal. However, for confined flows, a numerical boundary layer can appear and affect the velocity, depending on the lack of the orthogonality of the HHD. In fact, the projected velocity field does not contain such errors only if the boundary layer mode is orthogonal to the space of divergence-free vector fields. Orthogonality property is satisfied *a priori* for periodic channel flows therefore, the LES results concerning the spatially evolving boundary layer, i.e. a non-periodic channel flow, are illustrated. In this way, the effects of the lack of orthogonality and the benefits of the new

[‡]It can be shown that the orthogonal decomposition admits a unique solution in case of either tangential condition or normal condition assignments.

proposal can be clearly highlighted. The main conclusion of this study is that the higher order of accuracy in the intermediate boundary conditions is required since they allows us to get a more rapidly convergent solutions as well as less dissipation in the walls stresses.

2. THE PRESSURE-FREE PROJECTION METHODOLOGY FOR LES

The present paper focuses only on the so-called PFP method [7, 8, 10, 11], which is adopted for solving the LES equations for incompressible flows. For unconfined flows, this method is a second-order time-accurate version of the original Chorin's method [4, 14]. The guidelines of PFP method will be now generally addressed.

Consider the point-wise NS equations for isothermal, incompressible, Newtonian, viscous fluids, in a finite domain Ω, with smooth boundary $\partial\Omega$, written in dimensional form:

$$\underline{\nabla} \cdot \mathbf{v} = 0 \tag{1}$$

$$\frac{\partial \mathbf{v}}{\partial t} + \underline{\nabla} \cdot (\mathbf{v}\mathbf{v}) + \underline{\nabla} p' = \underline{\nabla} \cdot (2\nu \mathbf{D}) \tag{2}$$

$\mathbf{D} \triangleq \underline{\nabla}^s \mathbf{v}$ being the symmetric velocity gradient having zero trace (constraint (1) allows to get $\underline{\nabla} \cdot (2\nu\mathbf{D}) = \nu \nabla^2 \mathbf{v}$), ν is the kinematics viscosity and $p' = p/\rho_0$ with p the static pressure.

The mathematical problem consists in finding the vector fields $\mathbf{v}(\mathbf{x}, t)$ and $\underline{\nabla} p'(\mathbf{x}, t)$ satisfying (1), (2) in $\Omega' = \Omega \times (t_0, t)$ for given initial $\mathbf{v}(\mathbf{x}, t_0)$ and assigned boundary conditions $\mathbf{v}_\partial(t)$, while satisfying compatible conditions e.g. see Reference [21].

As well known, the LES approach is based on a formal separation between large- and small-scale flow components. If one considers only spatial scales separation then the application of a filtering procedure is represented, in physical space, as a convolution product of the velocity field with some suitable function G

$$\bar{\mathbf{v}}(\mathbf{x}, t) = \int_{\mathfrak{R}} G(\mathbf{x} - \mathbf{x}'; \Delta)\, \mathbf{v}(\mathbf{x}', t)\, \mathrm{d}\mathbf{x}' \tag{3}$$

being Δ a characteristic filter width.

For the sake of simplicity, only uniform filters are considered, thus filtering operation and spatial derivatives will commute. Otherwise, special filtering must be adopted [1]. Equations (1), (2) can be rewritten according to a well-known decomposition of the non-linear term (e.g. see Reference [1]) as

$$\underline{\nabla} \cdot \bar{\mathbf{v}} = 0 \tag{4}$$

$$\frac{\partial \bar{\mathbf{v}}}{\partial t} + \underline{\nabla} \cdot \overline{(\bar{\mathbf{v}}\bar{\mathbf{v}})} + \underline{\nabla} \overline{p'} = \underline{\nabla} \cdot (2\nu \bar{\mathbf{D}}) - \underline{\nabla} \cdot \bar{\mathbf{T}} \tag{5}$$

$\mathbf{T} = \mathbf{v}\mathbf{v} - \bar{\mathbf{v}}\bar{\mathbf{v}}$ being the exact SGS tensor term to be modelled for closing system (4), (5) and $\bar{\mathbf{D}} \triangleq \underline{\nabla}^s \bar{\mathbf{v}}$ is the filtered symmetric tensor.

According to the Bousinnesq sub-grid viscosity concept, the tensor $\mathbf{T}$ is modelled similarly to that of the molecular diffusion, that is like a stress term wherein the molecular viscosity ν is replaced by a point-wise time-dependent viscosity. This time-dependent viscosity is hereafter

denoted by ν_{LES} and will be expressed in terms of the resolved velocity $\bar{\mathbf{v}}$. Thus, the modelled SGS tensor $\bar{\mathbf{T}}_{\mathrm{d}}$ is defined by the approximation

$$\bar{\mathbf{T}} - \mathbf{I}\frac{\mathrm{Tr}(\bar{\mathbf{T}})}{3} \cong \bar{\mathbf{T}}_{\mathrm{d}} \equiv -2\nu_{\mathrm{LES}}\bar{\mathbf{D}} \tag{6}$$

where $\mathrm{Tr}(\bar{\mathbf{T}})$ stands for the trace of the tensor, $\bar{\mathbf{T}}_{\mathrm{d}}$ for the modelled deviatoric part and $\mathbf{I}$ is the identity operator.

Expression (6) is justified since, having the tensor $\bar{\mathbf{D}}$ zero trace, the same must happen to the modelled tensor $\bar{\mathbf{T}}_{\mathrm{d}}$. Therefore, the complementary spherical tensor is added to the filtered static pressure $\overline{p'}$ defining the new pressure variable $\bar{\pi} \equiv \overline{p'} + \mathrm{Tr}(\bar{\mathbf{T}})/3$. Let us remark that other SGS models are commonly used along with the eddy viscosity models, for example the scale similarity one but, for the specific aim of this paper, they are not pursued. The closure of the problem is obtained when a relation $\nu_{\mathrm{LES}} = \nu_{\mathrm{LES}}(\bar{\mathbf{v}})$ is specified, that is when a particular turbulence model is adopted. In this paper only the Smagorinsky model will be adopted. Such model is based on the energy equilibrium hypothesis and prescribes the viscosity as $\nu_{\mathrm{LES}} = (C\Delta)^2|\bar{\mathbf{D}}|$, where $|\bar{\mathbf{D}}| = (2\bar{D}_{ij}\bar{D}_{ij})^{1/2}$, C the Smagorinsky constant[§] and Δ a suitable length related to the filter width.

Finally, the system to be solved is constituted by the filtered momentum equation:

$$\frac{\partial \bar{\mathbf{v}}}{\partial t} + \underline{\nabla} \cdot \overline{(\bar{\mathbf{v}}\bar{\mathbf{v}})} + \underline{\nabla}\bar{\pi} = \underline{\nabla} \cdot (2\nu\bar{\mathbf{D}} - \bar{\mathbf{T}}_{\mathrm{d}}) \tag{7}$$

along with the continuity constraint (4).

For LES equations the mathematical problem consists in finding the vector fields $\bar{\mathbf{v}}(\mathbf{x}, t)$ and $\underline{\nabla}\bar{\pi}(\mathbf{x}, t)$ satisfying Equations (4) and (7) in $\Omega' = \Omega \times (t_0, t)$ for given initial $\bar{\mathbf{v}}(\mathbf{x}, t_0)$ and boundary conditions $\bar{\mathbf{v}}_\partial(t)$ assigned along the whole frontier $\partial\Omega$. It is assumed that is possible to deduce the boundary conditions $\bar{\mathbf{v}}_\partial(t)$ by filtering the velocity $\mathbf{v}$ along the frontier, although this topic is not trivial, e.g. see Reference [22]. As happens for the unfiltered NS equations, there is no thermodynamic pressure law, the scalar field $\bar{\pi}$ acting only as a Lagrangian multiplier.

A velocity–pressure decoupling is performed to avoid heavy computational efforts. One of the possible splitting methodologies is based on the HHD theorem of a vector field in a finite domain [2–6]. First, the AB/CN scheme is applied to Equation (7) in the time interval (t^n, t^{n+1}), leading to:

$$\begin{gathered}\left[I - \frac{\Delta t}{2}\underline{\nabla} \cdot (2\nu\underline{\nabla}^s)\right]\bar{\mathbf{v}}^{n+1} = \left[I + \frac{\Delta t}{2}\underline{\nabla} \cdot (2\nu\underline{\nabla}^s)\right]\bar{\mathbf{v}}^n \\ -\frac{\Delta t}{2}\underline{\nabla} \cdot (3\bar{\mathbf{H}}^n - \bar{\mathbf{H}}^{n-1}) - \Delta t\langle\widehat{\underline{\nabla} \cdot \bar{\mathbf{T}}_{\mathrm{d}}}\rangle_n^{n+1} - \int_{t^n}^{t^{n+1}} \underline{\nabla}\bar{\pi}\,\mathrm{d}t + O(\Delta t^3), \quad \mathbf{x} \in \Omega \\ \bar{\mathbf{v}}_\partial^{n+1} = g(\bar{\mathbf{v}}), \quad \mathbf{x} \in \partial\Omega\end{gathered} \tag{8}$$

[§]At present, most of LES computations are performed by means of the *dynamic model*, which permits to compute this viscosity as a function of space and time by means of a procedure [1] involving a test filter having a characteristic width $\Delta' > \Delta$.

having posed $\mathbf{H}=\bar{\mathbf{v}}\bar{\mathbf{v}}$ while $\Delta t\widehat{\langle\underline{\nabla}\cdot\bar{\mathbf{T}}_{\mathrm{d}}\rangle}_n^{n+1}\equiv\int_{t^n}^{t^{n+1}}\underline{\nabla}\cdot\bar{\mathbf{T}}_{\mathrm{d}}\,\mathrm{d}t+O(\Delta t^3)$ indicates a second-order discretization of the SGS time integral to be chosen between the CN or the AB scheme. It is assumed that the field $\bar{\mathbf{v}}^{n-1}$ is known and satisfies the continuity constraint $\underline{\nabla}\cdot\bar{\mathbf{v}}^{n-1}=0$.

Starting from Equation (8), the PFP method proceeds by disregarding the time integral of $\underline{\nabla}\bar{\pi}$, then solving the corresponding truncated prediction equation for an intermediate non-solenoidal velocity $\mathbf{v}^*$:

$$\begin{aligned}\left[I-\frac{\Delta t}{2}\underline{\nabla}\cdot(2\nu\underline{\nabla}^s)\right]\mathbf{v}^*&=\left[I+\frac{\Delta t}{2}\underline{\nabla}\cdot(2\nu\underline{\nabla}^s)\right]\bar{\mathbf{v}}^n\\&-\frac{\Delta t}{2}\underline{\nabla}\cdot(3\bar{\mathbf{H}}^n-\bar{\mathbf{H}}^{n-1})-\Delta t\widehat{\langle\underline{\nabla}\cdot\bar{\bar{\mathbf{T}}}_{\mathrm{d}}\rangle}_n^*,\quad\mathbf{x}\in\Omega\\\mathbf{v}_\partial^*&=f(\bar{\mathbf{v}}),\quad\mathbf{x}\in\partial\Omega\end{aligned}\tag{9}$$

At this stage, the intermediate velocity field $\mathbf{v}^*$ has no other meaning than that of an auxiliary variable at a fixed time, not corresponding to the velocity field $\bar{\mathbf{v}}$ at any time. Therefore, the NS system cannot tell us how to prescribe the intermediate boundary condition $\mathbf{v}_\partial^*$.

After having solved (9), the second step consists in determining an auxiliary gradient field such that $\mathbf{v}^*=\bar{\mathbf{v}}^{n+1}+\Delta t\underline{\nabla}\phi^{n+1}$ is the decomposition prescribed by the HHD theorem. However, as addressed in References [10, 11], the orthogonality of this decomposition, that is $\int_\Omega\bar{\mathbf{v}}^{n+1}\cdot\underline{\nabla}\phi^{n+1}\,\mathrm{d}V=0$, is not always guaranteed but depends on the prescribed boundary condition $\mathbf{n}\cdot\bar{\mathbf{v}}_\partial^{n+1}$, where $\mathbf{n}$ is the normal to the boundary oriented in outward direction.

Thus, by solving the Poisson problem

$$\begin{aligned}\nabla^2\phi^{n+1}&=\frac{1}{\Delta t}\underline{\nabla}\cdot\mathbf{v}^*,\quad\mathbf{x}\in\Omega\\\mathbf{n}\cdot\underline{\nabla}\phi_\partial^{n+1}&=\frac{1}{\Delta t}\mathbf{n}\cdot(\mathbf{v}_\partial^*-\bar{\mathbf{v}}_\partial^{n+1}),\quad\mathbf{x}\in\partial\Omega\end{aligned}\tag{10}$$

the intermediate velocity is projected onto the space of divergence-free vector fields and the continuity constraint (4) is then enforced.

As already addressed in the Introduction, in order for problem (10) to be well posed it is sufficient to prescribe that the normal component $\mathbf{n}\cdot\mathbf{v}_\partial^*$, equals the normal component of the gradient field, i.e. $\Delta t(\mathbf{n}\cdot\underline{\nabla}\phi_\partial^{n+1})$, added with that of the exact velocity, i.e. $\mathbf{n}\cdot\bar{\mathbf{v}}_\partial^{n+1}$. In other words, in order to ensure the continuity constraint (4), is not necessary to prescribe $\mathbf{n}\cdot\mathbf{v}_\partial^*$ but is only sufficient to set in the boundary condition $(10)_2$ the correct term $\mathbf{n}\cdot\bar{\mathbf{v}}_\partial^{n+1}$, whereas no one of the other two terms needs to be singularly prescribed. This feature is wholly consistent to the fact that the HHD is well posed with only one condition and such condition is expressed in terms of the physical value of the normal velocity component on the boundary. In fact, problem (10) is fully equivalent to the Poisson problem $\nabla^2\phi^{n+1}=(1/\Delta t)\underline{\nabla}\cdot\hat{\mathbf{v}}^*,\mathbf{x}\in\Omega$, but having a source term modified in such a way that the vector field $\hat{\mathbf{v}}^*$ assumes the value $\mathbf{n}\cdot\hat{\mathbf{v}}_\partial^*=\mathbf{n}\cdot\bar{\mathbf{v}}_\partial^{n+1}$ along the boundary, see References [10, 11], closed with homogeneous Neumann boundary conditions $\mathbf{n}\cdot\underline{\nabla}\phi_\partial^{n+1}=0,\mathbf{x}\in\partial\Omega$. Therefore, an important conclusion is that satisfying the continuity constraint in DNS/LES approaches, with projection methods, does not involve the assignment of the intermediate boundary conditions. Other details of such issue can be found in References [10, 11].

Eventually, the solution of problem (10) (which guarantees the existence of the HHD) allows us to perform the correction (i.e. the third step) of the intermediate velocity

$$\bar{\mathbf{v}}^{n+1} = \mathbf{v}^* - \Delta t \underline{\nabla} \phi^{n+1}, \quad \mathbf{x} \in \Omega \tag{11}$$

ensuring the final divergence-free velocity. It is immediate to see that when Equation (11) is projected along a boundary, only the normal component is verified but the tangential ones are not. This issue will be object of specific analysis in the next sections.

At this point, a first fundamental observation (valid for both DNS/LES) to be done is that the used notation $\underline{\nabla}\phi^{n+1}$ (i.e. adopting the superscript $n+1$) specifies only that the auxiliary gradient field provides the correction to enforce continuity at time t^{n+1} but *does not indicate* that there exists a time-continuous field $\phi(t)$ of which $\underline{\nabla}\phi^{n+1}$ constitutes a value at t^{n+1}. Actually, as it will be explained, this observation extends to the intermediate velocity field $\mathbf{v}^*$, too. Such a couple of issues are extensively illustrated in Section 4.2. Although other projection methods, for example the *incremental pressure* one [8, 15, 19, 20], retain a previous gradient $\underline{\nabla}\phi^n$ in the prediction equation, anyway this fact does not indicate that in such cases the function is assumed to be continuous in time.

A second fundamental observation (valid for LES) is that the real meaning of the velocity field $\mathbf{v}^*$ in Equation (9) will formally depend on the type of time integration adopted for $\bar{\mathbf{T}}_\mathrm{d}$. Indeed, depending on the type of time discretization of $\bar{\mathbf{T}}_\mathrm{d}$, chosen between CN or AB formulas, one will set either the relation $\nu_\mathrm{LES} = f(\mathbf{v}^*, \bar{\mathbf{v}}^n)$ or $\nu_\mathrm{LES} = f(\bar{\mathbf{v}}^n, \bar{\mathbf{v}}^{n-1})$. Thus, the statement of the problem described in this paper is expressed as

Depending on the type of discrete time integration applied to the SGS tensor $\bar{\mathbf{T}}_\mathrm{d}$, which are the congruent second-order time-accurate intermediate boundary conditions $(9)_2$ to be specified?

The next sections will provide some answers to these issues.

3. TIME INTEGRATION OF THE SGS TENSOR: INTERMEDIATE VELOCITY AND AUXILIARY GRADIENT FIELD

Owing to the similarity of the eddy viscosity SGS tensor (6) with the molecular diffusive one, it is straightforward to suppose that the CN integration can be a good choice in Equation (8), that is assuming $\Delta t \widehat{\langle \underline{\nabla} \cdot \bar{\mathbf{T}}_\mathrm{d} \rangle}_n^{n+1} = (\Delta t/2) \underline{\nabla} \cdot (\bar{\mathbf{T}}_\mathrm{d}^{n+1} + \bar{\mathbf{T}}_\mathrm{d}^n)$. Thus, since in Equation $(9)_1$ the pressure term has been disregarded, one has $\Delta t \widehat{\langle \underline{\nabla} \cdot \bar{\mathbf{T}}_\mathrm{d} \rangle}_n^* = (\Delta t/2) \underline{\nabla} \cdot (\bar{\mathbf{T}}_\mathrm{d}^* + \bar{\mathbf{T}}_\mathrm{d}^n)$ with $\bar{\mathbf{T}}_\mathrm{d}^* = -2\nu_\mathrm{LES}^* \underline{\nabla}^s \mathbf{v}^*$. Hence, problem (9) rewrites as

$$\begin{aligned} \left[I - \frac{\Delta t}{2} \underline{\nabla} \cdot (2\nu_t^* \underline{\nabla}^s) \right] \mathbf{v}^* &= \left[I + \frac{\Delta t}{2} \underline{\nabla} \cdot (2\nu_t^n \underline{\nabla}^s) \right] \bar{\mathbf{v}}^n + \\ &- \frac{\Delta t}{2} \underline{\nabla} \cdot (3\bar{\mathbf{H}}^n - \bar{\mathbf{H}}^{n-1}), \quad \mathbf{x} \in \Omega \\ \mathbf{v}_\partial^* &= f_\mathrm{CN}(\bar{\mathbf{v}}), \quad \mathbf{x} \in \partial\Omega \end{aligned} \tag{12}$$

where the total viscosity $\nu_t = \nu + \nu_\mathrm{LES}$, that is a function of time and space, was defined. Therefore, $\nu_t^* = \nu + \nu_\mathrm{LES}^*$, where $\nu_\mathrm{LES}^* = \nu_\mathrm{LES}^*(\mathbf{v}^*) = (C\Delta)^2 |\mathbf{D}^*|$, and Equation (12) is a genuine

non-linear problem. The notation f_{CN} has been adopted to highlight the fact that the intermediate boundary condition must account for the CN type of SGS integration.

Conversely it is also possible to discretize the time integral in Equation (8) by means of the AB integration, that is $\Delta t\widehat{\langle\underline{\nabla}\cdot\bar{\mathbf{T}}_{\mathrm{d}}\rangle_n}^{n+1}=(\Delta t/2)\underline{\nabla}\cdot(3\bar{\mathbf{T}}_{\mathrm{d}}^{n}-\bar{\mathbf{T}}_{\mathrm{d}}^{n-1})$, in accordance to the type of integration used for the advective terms. In this case one can rewrite (9) by taking into account that now the SGS model does not longer depends on $\mathbf{v}^*$:

$$\begin{gathered}\left[I-\frac{\Delta t}{2}\underline{\nabla}\cdot(2\nu\underline{\nabla}^s)\right]\mathbf{v}^*=\left[I+\frac{\Delta t}{2}\underline{\nabla}\cdot(2\nu\underline{\nabla}^s)\right]\bar{\mathbf{v}}^n+\\ -\frac{\Delta t}{2}\underline{\nabla}\cdot[3(\bar{\mathbf{H}}^n+\bar{\mathbf{T}}_{\mathrm{d}}^n)-\bar{\mathbf{H}}^{n-1}-\bar{\mathbf{T}}_{\mathrm{d}}^{n-1}],\quad \mathbf{x}\in\Omega\\ \mathbf{v}_{\partial}^*=f_{\mathrm{AB}}(\bar{\mathbf{v}}),\quad \mathbf{x}\in\partial\Omega\end{gathered}\tag{13}$$

where $\bar{\mathbf{T}}_{\mathrm{d}}^n=-2\nu_{\mathrm{LES}}^n\bar{\mathbf{D}}^n,\bar{\mathbf{T}}_{\mathrm{d}}^{n-1}=-2\nu_{\mathrm{LES}}^{n-1}\bar{\mathbf{D}}^{n-1}$. The notation f_{AB} now highlights the fact that the intermediate boundary condition must account for the multi-step explicit SGS integration. This time Equation (13) has the attractive feature of leading to a linear algebraic system.

Both equations show that the intermediate velocity $\mathbf{v}^*$ accounts differently for both filtering and SGS modelling. In a rigorous formalism (here avoided), one should differentiate each time the symbol for the velocity $\mathbf{v}^*$ highlighting the discrete equation from which it comes. The differences between (12) and (13) consist in both numerical and mathematical characterization. Hence, numerical boundary conditions $(12)_2$ or $(13)_2$ cannot be the same but they must be specified depending on the adopted time integration.

Moreover, the gradient $\underline{\nabla}\phi^{n+1}$ relates in a different way to the real pressure gradient depending on which one between Equations (12) and (13) is used. In fact, if one adopts Equation (12), by substituting decomposition (11) and exploiting Equation (8), the functional relation between $\underline{\nabla}\bar{\pi}$ and $\underline{\nabla}\phi^{n+1}$ expresses as:

$$\underline{\nabla}\cdot[(\nu_{\mathrm{LES}}^{n+1}-\nu_{\mathrm{LES}}^*)\bar{\mathbf{D}}^{n+1}]+\left[I-\frac{\Delta t}{2}\underline{\nabla}\cdot(2\nu_t^*\underline{\nabla}^s)\right]\underline{\nabla}\phi_{\mathrm{CN}}^{n+1}=\langle\underline{\nabla}\bar{\pi}\rangle_n^{n+1}\tag{14}$$

having defined the exact integral $\langle\underline{\nabla}\bar{\pi}\rangle_n^{n+1}\equiv(1/\Delta t)\int_{t^n}^{t^{n+1}}\underline{\nabla}\bar{\pi}\,\mathrm{d}t$ and used the subscript notation CN to indicate the auxiliary gradient field defined by the way of the CN scheme.

On the other hand, if one adopts Equation (13), after some manipulations, it expresses as

$$\left[I-\frac{\Delta t}{2}\underline{\nabla}\cdot(2\nu\underline{\nabla}^s)\right]\underline{\nabla}\phi_{\mathrm{AB}}^{n+1}=\langle\underline{\nabla}\bar{\pi}\rangle_n^{n+1}\tag{15}$$

having specified the subscript notation AB to indicate the auxiliary gradient field defined by the way of the AB scheme. Of course, the RHS of (14) and (15) is the same.

A key feature, highlighted by both (14) and (15), is that $\underline{\nabla}\phi^{n+1}$ relates to the time integral $\langle\underline{\nabla}\bar{\pi}\rangle_n^{n+1}$ by means of an $O(\Delta t)$ term. Thus, $\underline{\nabla}\phi^{n+1}$ is an auxiliary variable representing an integral contribution, not a time-continuous field. This aspect will be better addressed into the next sections. Furthermore, observe that Equation (15) is similar to the relation derived for the unfiltered NS equations, e.g. see References [7, 8, 10, 11], while Equation (14), involves also the SGS modelling.

In conclusion it will be necessary to take into account the type of SGS time integration, i.e. (14) or (15), then consider $\overline{p'} = \bar{\pi} - \mathrm{Tr}(\bar{\mathbf{T}})/3$, to reconstruct the real pressure from the field $\underline{\nabla}\phi^{n+1}$.

4. TIME-ACCURATE INTERMEDIATE BOUNDARY CONDITIONS

According to the HHD theorem, only one condition is required therefore, nothing can be ensured for the tangential velocity component. Of course, this is due to the potential character of the auxiliary variable ϕ^{n+1}. The uncertainty arises from the rotational part of the solution, namely directly from the intermediate velocity computed from Equation (12) or (13). In fact, by projecting decomposition (11) along the tangential direction to the boundary, one must ensure that $\mathbf{t}\cdot\bar{\mathbf{v}}_\partial^{n+1} = \mathbf{t}\cdot(\mathbf{v}_\partial^* - \Delta t\underline{\nabla}\phi|_\partial^{n+1})$ where $\mathbf{t}\cdot\mathbf{v}_\partial^*$ is the boundary values already prescribed in the prediction step and $\mathbf{t}\cdot\underline{\nabla}\phi|_\partial^{n+1}$ depends on the solution of problem (10). The difficulty is in the fact that since $\mathbf{t}\cdot\mathbf{v}_\partial^*$ must be prescribed (first step) before that $\underline{\nabla}\phi^{n+1}$ is available (second step), an approximate expression of the type $\mathbf{t}\cdot\mathbf{v}_\partial^* = \mathbf{t}\cdot\bar{\mathbf{v}}_\partial^{n+1} + \Delta t\mathbf{t}\cdot\mathbf{f}(\phi)|_\partial$ is generally adopted, $\mathbf{f}$ being only some approximation of the auxiliary field $\underline{\nabla}\phi^{n+1}$. As a consequence, the tangential velocity component is second-order accurate if $\mathbf{t}\cdot(\mathbf{f}(\phi)|_\partial - \underline{\nabla}\phi|_\partial^{n+1}) = O(\Delta t^2)$ verifies at the end of the projection step (third step). Actually, it will be shown in the next section that one of the most-used intermediate boundary conditions is only first-order time-accurate.

It is usually reputed sufficient to prescribe boundary conditions, which are one order of accuracy lower than that into the interior. This was shown for hyperbolic equations in Reference [23] and results from maximum principle for linear parabolic equations. On the other hand, practical computations reveal that such lower order of accuracy can also lead to a large increasing of the error, spreading in the interior. Regardless of the rate of convergence, the errors on any grid points may be greater than required [24, 25]. This can become unacceptable for an accurate computation of relevant variables as the stresses on a wall. Furthermore, in practical computational codes, the obtained tangential components are simply disregarded and reset to their known values on the boundary at the end of each time-step. However, this strategy was proved to remain still inadequate, as well as it can reduce the smoothness of the velocity field [8, 9].

All these problems become much more complicated for LES, as $\mathbf{v}^*$ must also account for SGS modelling. Therefore, specific care must be devoted to the assignment of the tangential velocities in $(12)_2$ or $(13)_2$ as the stresses on the boundaries are altered by a first-order truncation error. As a final goal, the boundary conditions for $\mathbf{v}^*$ should be consistent to the projection step, although at the time they are applied, the function $\underline{\nabla}\phi^{n+1}$ is not yet known.

4.1. Taylor series-based boundary conditions

One of the most adopted formulations for prescribing the intermediate boundary conditions is the one proposed for the unfiltered NS equations in Reference [7]. Kim and Moin, following a procedure of LeVeque [24], proposed to specify a non-homogeneous intermediate boundary conditions by hypothesising that a unique *time-continuous* field $\mathbf{v}^*(t)$ exists. This is done although the auxiliary field $\mathbf{v}^*$ has been introduced only as a mathematical position into the time-discretized prediction momentum and, as already discussed, its meaning depends on this discretization. Such type of boundary conditions has been supposed to produce quite accurate

results and has been largely used also for LES computations. Let us briefly address the procedure for the unfiltered NS equations.

The approach was based on a Taylor series expansion about t^n according to $\mathbf{v}^{*n+1} = \mathbf{v}^{*n} + \Delta t(\partial \mathbf{v}^*/\partial t)|^n + O(\Delta t^2)$. Observe that, in doing so, it was implicitly assumed to distinguish two time levels for the provisional field, i.e. $\mathbf{v}^{*n+1} \equiv \mathbf{v}^*$ and $\mathbf{v}^{*n}$, during the same time interval. Since the intermediate field $\mathbf{v}^*$ is supposed to be a time-continuous field, its time derivative is expressed from a differential equation derived from Equation (2) that is $\partial \mathbf{v}^*/\partial t = \underline{\nabla} \cdot (-\mathbf{v}^*\mathbf{v}^* + 2\nu \underline{\nabla}^s \mathbf{v}^*)$.

However, the initial condition is chosen such that $\mathbf{v}^{*n} = \mathbf{v}^n$ thus, one gets $(\partial \mathbf{v}^*/\partial t)|^n = \underline{\nabla} \cdot (-\mathbf{v}^n\mathbf{v}^n + 2\nu \underline{\nabla}^s \mathbf{v}^n) = (\partial \mathbf{v}/\partial t)|^n + \underline{\nabla} p'^n$ and the Taylor series rewrites as $\mathbf{v}^* = \mathbf{v}^n + \Delta t(\partial \mathbf{v}/\partial t)|^n + \Delta t \underline{\nabla} p'^n + O(\Delta t^2) = \mathbf{v}^{n+1} + \Delta t \underline{\nabla} p'^n + O(\Delta t^2)$. Finally, the first-order relation $\underline{\nabla} p'^n = \underline{\nabla} \phi^n + O(\Delta t)$ is exploited and one has the final expression

$$\boxed{\mathbf{v}^*_\partial = \mathbf{v}^{n+1}_\partial + \Delta t \underline{\nabla} \phi|^n_\partial + O(\Delta t^2)} \tag{16}$$

meaning that $\mathbf{f}(\phi)|_\partial = \underline{\nabla} \phi|^n_\partial$ is assumed. This means that also the scalar function ϕ must be considered a time-continuous field. The gradient of the ϕ^n along the boundary is therefore required, for this formula to be useful.

Actually, one comes into two possible kinds of errors:

(a) A numerical boundary layer. This comes because $\mathbf{n} \cdot \underline{\nabla} \phi^{n+1} = \mathbf{n} \cdot \underline{\nabla} \phi^n = \cdots = \mathbf{n} \cdot \underline{\nabla} \phi^0$ on $\partial\Omega$ is implicitly prescribed.
(b) A slip condition error. Supposing for ϕ a time-continuous function, this is because it results $\mathbf{t} \cdot (\underline{\nabla} \phi|^n_\partial - \underline{\nabla} \phi|^{n+1}_\partial) = O(\Delta t)$.

Many analyses of the original first-order time-accurate Chorin's method highlighted the appearance of the numerical boundary layer, generated by mismatch in the boundary conditions for $\mathbf{v}^*$ when the domain is confined. Modal analyses have demonstrated that a numerical boundary layer is generated even when the second-order accurate AB/CN integration is adopted [9, 14–19].

E and Liu [15, 16] stated that the effect of solid boundaries does not result restricted to create numerical boundary layers. In fact these latter introduce high-frequency oscillations reducing the order of the accuracy even in the interior of the domain. Specifically, Dirichlet boundary conditions for the pressure were shown to lead to $O(1)$ numerical boundary layers. They performed the analysis by supposing a physical boundary layer approximation, that is prescribing $(\partial p/\partial n)|^{n+1}_\partial = 0$ while considering $\mathbf{n} \cdot \mathbf{v}^*_\partial = 0$ in the prediction step. However, in this way, the differences from the real pressure gradient and the auxiliary gradient field defined into (14), (15) are not clearly highlighted.

More recently, Strikwerda and Lee [9] stated from their modal analysis that the numerical boundary layer really is in the auxiliary variable ϕ, not in the pressure. Then, Brown *et al.* [8] showed that a first-order convergence in the pressure is numerically obtained whatever is the prescribed value $\mathbf{n} \cdot \mathbf{v}^*_\partial$, as long as respecting (10). This is obtained despite the second-order convergence predicted by the normal mode analysis. They adduced this lack in convergence rate to the non-smoothness of the field $\mathbf{v}^*$ close to the boundary, that results in the non-smoothness also for the variable ϕ. As a remedy to this error they proposed to adopt inhomogeneous Neumann boundary conditions.

However it can be shown that, at least in case of prescribed periodical condition, in order to retain the second-order accuracy in the velocity, the knowledge of the authentic pressure gradient field is never required. It is generally accepted that, owing to the peculiar construction of the PFP method, the limited accuracy of the gradient field does not limit the accuracy in the velocity. This is because the pressure error at any time-step is disregarded [8] while prohibiting that it could accumulate in time and contribute in the momentum equation solution.

For different prescription of the boundary conditions (e.g. confined flows), to retain fully second-order accuracy all the way up to the boundary (despite the first-order pressure error highlighted by (14), (15)) it is necessary to proceed in such a way that the produced numerical boundary layer does not affect the velocity. Actually, the projected velocity field $\mathbf{v}^{n+1}$ does not contain such errors if this boundary layer mode is orthogonal to the space of divergence-free vector fields. Thus, a crucial issue consists in fulfilling orthogonality of decomposition (11). At the same time it is necessary to obtain sufficiently smooth slip conditions. Unfortunately, it is not always possible to satisfy such a condition, which corresponds to perform an orthogonal projection, e.g. see References [10, 11]. Hence, it is suggested that if the boundary layer mode is an exact gradient it does not contribute in altering the divergence-free velocity field.

4.2. Extension of the Taylor series approach to LES equations

Thus, coming back to the present LES analysis, an important aspect to be first highlighted is that the notation $\underline{\nabla}\phi^n$ used in Equation (16) is someway misleading. In fact, in the generic time interval (t^n, t^{n+1}) wherein one wants to determine $\mathbf{v}^*$ by means of Equation (12) or (13), the intermediate velocity at t^n is set to $\mathbf{v}^{*n} = \bar{\mathbf{v}}^n$. Hence, as the functions $\mathbf{v}^*$ and $\underline{\nabla}\phi$ are supposed continuous, decomposition (11) should apply at any time in the interval and it would be proper to set $\underline{\nabla}\phi^n = \mathbf{0}$. Let us recall that the PFP method exploits the auxiliary fields $\mathbf{v}^*$ and $\underline{\nabla}\phi^{n+1}$ only in a discrete sense as highlighted by Equations (12), (14) and (13), (15). Therefore, one must be aware that, despite of the guesswork, $\underline{\nabla}\phi^n$ in (16) *cannot stand for the value of a continuous function at the time* t^n in the time interval (t^n, t^{n+1}).

Actually, Equation (16) is practically implemented in computational codes by using the field $\underline{\nabla}\phi^n$ which is computed and then saved from the previous time-integration step that is performed in the interval (t^{n-1}, t^n). Such field must be more properly related to the exact integral $\langle \underline{\nabla}\bar{\pi} \rangle_{n-1}^n$. This concept is valid for any value[¶] $\underline{\nabla}\phi^0, \underline{\nabla}\phi^1, \ldots$ and it should be now clear that the auxiliary gradient field could not be straightforwardly manipulated as a unique continuous function of time. This issue must be considered when extending proposal (16) to higher terms. To the best of the author's knowledge, this specific feature of the auxiliary variable $\underline{\nabla}\phi$ does not seem to have been sufficiently highlighted in the literature. Only recently, during the revision stage of this paper, it appeared in Reference [26] a continuous projection method that accords with the continuous approach presented in Reference [10].

Moreover, some other considerations arise from expression (16):

(a) It must be redefined for the LES equations, not for the unfiltered NS equations.
(b) The truncation of the adopted Taylor expansion is not congruent to the local truncation error of the AB/CN time integration, that is $O(\Delta t^2)$ in a single time-step.

[¶]The initial gradient field is arbitrary.

The goal is to derive the $O(\Delta t^3)$ accurate Taylor series-based boundary conditions (i.e. fully congruent to the second-order accuracy of the AB/CN) in the framework of LES equations. Therefore, the approach used in References [10, 11] is now extended.

According to the Taylor expansion for $\mathbf{v}^*$, this time written up to the second-order term, one has

$$\mathbf{v}^* = \mathbf{v}^{*n} + \Delta t \left.\frac{\partial \mathbf{v}^*}{\partial t}\right|^n + \frac{\Delta t^2}{2}\left.\frac{\partial^2 \mathbf{v}^*}{\partial t^2}\right|^n + O(\Delta t^3) \tag{17}$$

wherein one must substitute the congruent expressions for the time derivatives of $\mathbf{v}^*$ but now derived from the filtered momentum quantity equation. Such goal requires to make the fundamental distinction between the differential equation to which Equation (12) or (13) tends to for vanishing time-steps. Again, this task is necessary, as in the PFP method *the intermediate velocity exists only in a discrete sense*. The real meaning of $\mathbf{v}^*$ depends on which one is the chosen time discretized equation, while it would result erroneous to consider for both schemes a unique expression for the derivatives in (17).

Let us first rearrange Equation (7) in a more compact form as

$$\frac{\partial \bar{\mathbf{v}}}{\partial t} + \underline{\nabla} \cdot \bar{\mathbf{H}} + \underline{\nabla}\bar{\pi} = \underline{\nabla} \cdot (2\nu_t \bar{\mathbf{D}}) \tag{18}$$

then, it can be shown that Equation (12) is the consistent AB/CN time integration of this differential equation

$$\frac{\partial \mathbf{v}^*}{\partial t} = -\underline{\nabla} \cdot \bar{\mathbf{H}} + \underline{\nabla} \cdot (2\nu_t^* \mathbf{D}^*) \tag{19}$$

while Equation (13) results to be consistent to this other one:

$$\frac{\partial \mathbf{v}^*}{\partial t} = -\underline{\nabla} \cdot \bar{\mathbf{H}} + \underline{\nabla} \cdot (2\nu \mathbf{D}^*) + \underline{\nabla} \cdot (2\nu_{\mathrm{LES}} \bar{\mathbf{D}}) \tag{20}$$

Both equations, associated to the same initial condition $\mathbf{v}^{*n} = \bar{\mathbf{v}}^n$, describe the evolution of a field $\mathbf{v}^*$ but the two solutions are, generally, different, each one satisfying either (19) or (20). This way, the meaning of the discrete intermediate velocity can be correctly extended to that one of a continuous field in (t^n, τ). Clearly, on the basis of the previous considerations, Equations (19) and (20) must be exploited in each single time interval (t^n, t^{n+1}) where the auxiliary function $\mathbf{v}^*$ can be considered continuous. More rigorously, the field $\mathbf{v}^*$ remains continuous also in (t^{n+1}, τ) but it will be simply no longer used. In fact, the differential problem must be reset in the successive integration interval (t^{n+1}, t^{n+2}). Therefore, the set of successive integrations produces a family of auxiliary time-continuous functions as it is shown in Figures 1(a) and (b).

The key task is to be able of finding a relation for $\mathbf{v}_\partial^*$, starting from (17), while taking into account that one still does not know $\underline{\nabla}\phi^{n+1}$ at the time one computes $\mathbf{v}^*$. First, it is useful to rewrite Equations (19) and (20) by exploiting Equation (18) which is valid for both of them and eliminating the convective term $\mathbf{H}$ according to

$$\frac{\partial \bar{\mathbf{v}}}{\partial t} + \underline{\nabla}\bar{\pi} = \frac{\partial \mathbf{v}^*}{\partial t} - \underline{\nabla} \cdot (2\nu_t^* \mathbf{D}^*) + \underline{\nabla} \cdot (2\nu_t \bar{\mathbf{D}}) \tag{21}$$

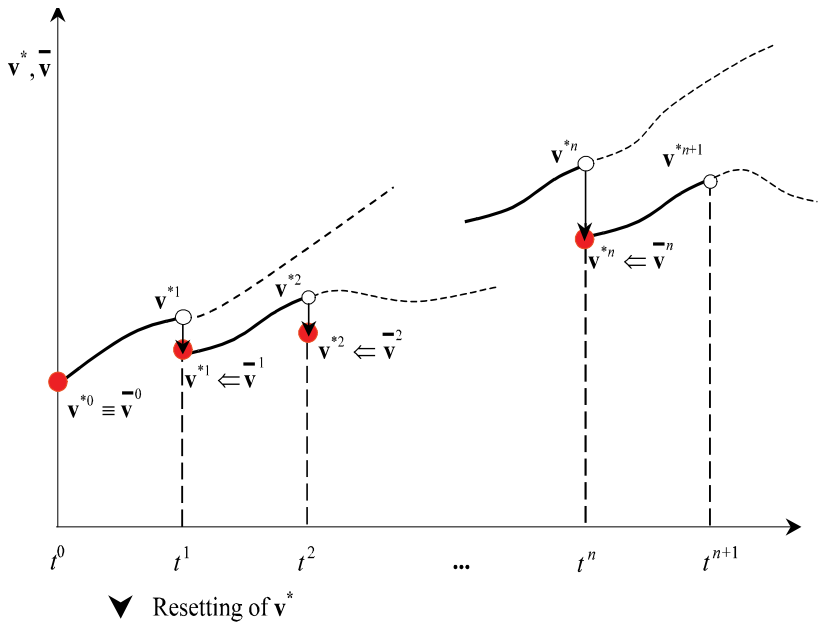

(a)

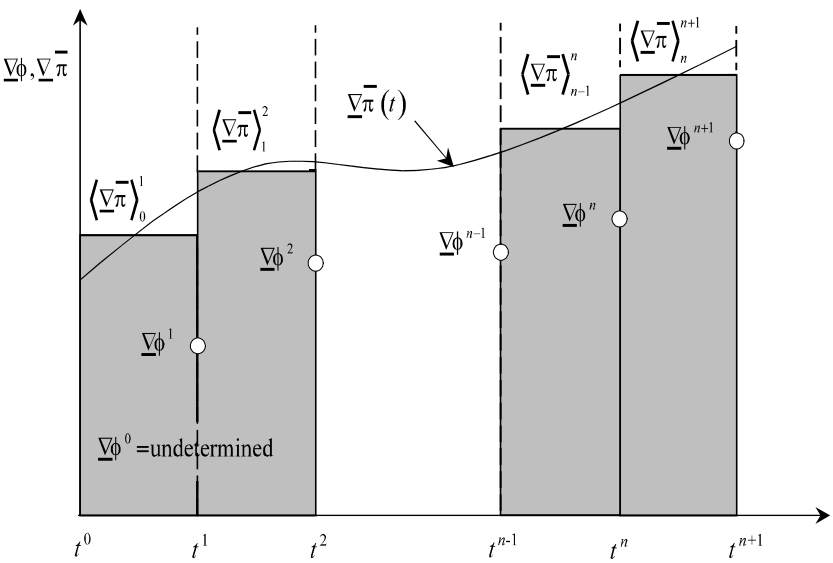

(b)

Figure 1. Sketch of the time integration process for the auxiliary: (a) velocity, see Equation (19) or (20); and (b) gradient, see Equation (14) or (15).

$$\frac{\partial \bar{\mathbf{v}}}{\partial t} + \underline{\nabla}\bar{\pi} = \frac{\partial \mathbf{v}^*}{\partial t} + \underline{\nabla} \cdot [2\nu(\bar{\mathbf{D}} - \mathbf{D}^*)] \tag{22}$$

respectively. It is easy to verify that, by assuming as initial condition the divergence-free vector field $\mathbf{v}^{*n} = \bar{\mathbf{v}}^n$, both (21) and (22), when evaluated at t^n, lead to this same expression for the first derivative

$$\left.\frac{\partial \bar{\mathbf{v}}}{\partial t}\right|^n + \underline{\nabla}\bar{\pi}^n = \left.\frac{\partial \mathbf{v}^*}{\partial t}\right|^n \tag{23}$$

It is very simple to reformulate the first-order accurate boundary conditions (16) in terms of the LES equation. After that Equation (23) is substituted into the Taylor expansion, one gets $\mathbf{v}^* = \bar{\mathbf{v}}^n + \Delta t((\partial \bar{\mathbf{v}}/\partial t)|^n + \underline{\nabla}\bar{\pi}^n) + O(\Delta t^2) = \bar{\mathbf{v}}^{n+1} + \Delta t \underline{\nabla}\bar{\pi}^n + O(\Delta t^2)$ thus, one has to suitably express $\underline{\nabla}\bar{\pi}^n$ in terms of the auxiliary gradient field that is available at the time in which the intermediate boundary conditions for $\mathbf{v}^*$ have to be applied.

Hence, one writes $\underline{\nabla}\bar{\pi}^n = \langle \underline{\nabla}\bar{\pi} \rangle_{n-1}^n + O(\Delta t)$ where $\langle \underline{\nabla}\bar{\pi} \rangle_{n-1}^n \equiv (1/\Delta t) \int_{t^{n-1}}^{t^n} \underline{\nabla}\bar{\pi}\, \mathrm{d}t$. When considering (14), but concerning the interval (t^{n-1}, t^n), one would obtain $\langle \underline{\nabla}\bar{\pi} \rangle_{n-1}^n = \underline{\nabla} \cdot [(v_{\mathrm{LES}}^n - v_{\mathrm{LES}}^*)\bar{\mathbf{D}}^n] + \underline{\nabla}\phi_{\mathrm{CN}}^n$, while considering (15) one would simply get $\langle \underline{\nabla}\bar{\pi} \rangle_{n-1}^n = \underline{\nabla}\phi_{\mathrm{AB}}^n$, having disregarded higher order terms in both relations. One must be careful that in the former expression, $v_{\mathrm{LES}}^n \neq v_{\mathrm{LES}}^*$ must be considered but v_{LES}^* is related to the auxiliary velocity field already computed in (t^{n-1}, t^n) that, therefore, must be saved.

This example showed only that the intermediate boundary condition for LES equation can be expressed from (16) while substituting either $\underline{\nabla}\phi_{\mathrm{CN}}^n$ or $\underline{\nabla}\phi_{\mathrm{AB}}^n$. As a matter of fact, also after considering the correct LES equations, the problem remains the same: along the boundary one has an order of accuracy lesser than into the interior. A remedy to this fact is now illustrated.

In order to develop higher order intermediate boundary conditions, it is necessary to expand the previous observations to the second-order term in (17). Depending on the chosen discrete time integration (12) or (13), the expression of the second-order derivative is not unique but must be expressed by means of time derivation of either Equation (21) or (22), respectively. It can be shown (for the sake of brevity the full details are not reported) that as far as the CN integration is concerned, one gets

$$\mathbf{v}_\partial^* = f_{\mathrm{CN}} = \bar{\mathbf{v}}_\partial^{n+1} + \Delta t \left[I + \frac{\Delta t}{2} \underline{\nabla} \cdot (2\nu_t^n \underline{\nabla}^s) \right] \Bigg|_\partial^n \underline{\nabla}\bar{\pi}^n + \frac{\Delta t^2}{2} \left\{ \underline{\nabla} \left. \frac{\partial \bar{\pi}}{\partial t} \right|^n \right.$$

$$\left. + 2\underline{\nabla} \cdot \left[\left(\left. \frac{\partial v_{\mathrm{LES}}^*}{\partial t} \right|^n - \left. \frac{\partial v_{\mathrm{LES}}}{\partial t} \right|^n \right) \bar{\mathbf{D}}^n \right] \right\} \Bigg|_\partial + O(\Delta t^3) \tag{24}$$

It appears that the difference $\mathbf{v}^* - \bar{\mathbf{v}}^{n+1}$ is not a pure gradient field since it is not possible in general to assess $(\partial v_{\mathrm{LES}}^*/\partial t)|^n - (\partial v_{\mathrm{LES}}/\partial t)|^n = O(\Delta t)$ on the boundaries. What is more, Equation (24) remains still to be linked to the field $\underline{\nabla}\phi_{\mathrm{CN}}^n$ by means of Equation (14), so leading to a complicate expression to be used for solving (12) with the congruent intermediate boundary condition. This conclusion, along with the fact that (12) should be carefully linearized, suggest us that is suitable to avoid the CN integration of the SGS term in the form expressed by Equation (12). Thus, other manipulations of such integration are not further considered in this paper and only the analysis of the AB scheme is focused.

4.3. Second-order accurate intermediate boundary conditions for the AB-based SGS time integration. Analysis of Equation (13)

From the time derivative of (22), which is the time-continuous differential equation for $\mathbf{v}^*$ consistent to the AB scheme, one gets

$$\frac{\partial^2 \mathbf{v}^*}{\partial t^2} = \frac{\partial^2 \bar{\mathbf{v}}}{\partial t^2} + \underline{\nabla}\frac{\partial \bar{\pi}}{\partial t} - \underline{\nabla}\cdot\left[2\nu\underline{\nabla}^s\left(\frac{\partial \bar{\mathbf{v}}}{\partial t} - \frac{\partial \mathbf{v}^*}{\partial t}\right)\right] \tag{25}$$

that, evaluated at time t^n while exploiting Equation (23), becomes

$$\left.\frac{\partial^2 \mathbf{v}^*}{\partial t^2}\right|^n = \left.\frac{\partial^2 \bar{\mathbf{v}}}{\partial t^2}\right|^n + \underline{\nabla}\left.\frac{\partial \bar{\pi}}{\partial t}\right|^n + \underline{\nabla}\cdot(2\nu\underline{\nabla}^s\underline{\nabla}\bar{\pi}^n) \tag{26}$$

Then, by substituting (23) and (26) into expansion (17), after some manipulations, it can be shown that one gets

$$\mathbf{v}^* = \bar{\mathbf{v}}^{n+1} + \Delta t\left[I + \frac{\Delta t}{2}\underline{\nabla}\cdot(2\nu\underline{\nabla}^s)\right]\underline{\nabla}\bar{\pi}^n + \frac{\Delta t^2}{2}\underline{\nabla}\left.\frac{\partial \bar{\pi}}{\partial t}\right|^n + O(\Delta t^3) \tag{27}$$

The main conclusion is that now, the difference $\mathbf{v}^* - \bar{\mathbf{v}}^{n+1}$ is a pure gradient field, provided that the commutation $[\underline{\nabla}\cdot(2\nu\underline{\nabla}^s)]\underline{\nabla}\bar{\pi}^n = \underline{\nabla}(\nu\nabla^2\bar{\pi}^n)$ applies. For continuous operator, this is true for unbounded flows whereas, for bounded ones, spatial discretization can inhibit commutation to remain valid. Thus, according to decomposition (11), one can deduce from comparison with Equation (27) that the auxiliary gradient field expresses as $\underline{\nabla}\phi_{\mathrm{AB}}^{n+1} = \underline{\nabla}(\bar{\pi}^n + (\nu\Delta t/2)\nabla^2\bar{\pi}^n) + (\Delta t/2)\underline{\nabla}(\partial\bar{\pi}/\partial t)|^n + O(\Delta t^2)$.

However, in order for expression (27) to be practically applicable as intermediate boundary conditions for (13), it is still necessary to reorganize it in terms of the only auxiliary field $\underline{\nabla}\phi_{\mathrm{AB}}$, evaluated at selected time-steps in which it is known. The knowledge of the auxiliary gradient fields allows us to know also the pressure gradients averaged in several time intervals, by means of repeated applications of (15) (see Figure 1(b)). Hence, one of the possible strategies is to express the entire unknown point-wise filtered pressure gradients in (27) in terms of the time-averaged counterpart, while taking care of retaining all second-order magnitude terms.

Since $\underline{\nabla}\bar{\pi}$ has been supposed a time-continuous function, the exact time-average in the interval (t^{n-1}, t^n) is expressed in terms of the point-wise gradient field as

$$\langle\underline{\nabla}\bar{\pi}\rangle_{n-1}^n = \underline{\nabla}\bar{\pi}^n - \frac{\Delta t}{2}\left.\frac{\partial \underline{\nabla}\bar{\pi}}{\partial t}\right|^n + O(\Delta t^2) \tag{28}$$

being, according to (15), $\langle\underline{\nabla}\bar{\pi}\rangle_{n-1}^n = [I - (\Delta t/2)\underline{\nabla}\cdot(2\nu\underline{\nabla}^s)]\underline{\nabla}\phi_{\mathrm{AB}}^n$ a known term at the current time-step. Furthermore, it is also possible to use the trapezoidal rule for expressing two successive time-averages

$$\langle\underline{\nabla}\bar{\pi}\rangle_{n-1}^n = \frac{\underline{\nabla}\bar{\pi}^n + \underline{\nabla}\bar{\pi}^{n-1}}{2} + O(\Delta t^2) \tag{29}$$

$$\langle\underline{\nabla}\bar{\pi}\rangle_{n-2}^{n-1} = \frac{\underline{\nabla}\bar{\pi}^{n-1} + \underline{\nabla}\bar{\pi}^{n-2}}{2} + O(\Delta t^2) \tag{30}$$

from which, one gets

$$\langle \underline{\nabla}\bar{\pi} \rangle_{n-1}^{n} - \langle \underline{\nabla}\bar{\pi} \rangle_{n-2}^{n-1} = \frac{\underline{\nabla}\bar{\pi}^{n} - \underline{\nabla}\bar{\pi}^{n-2}}{2} + O(\Delta t^2) \tag{31}$$

This last relation, along with Equation (28), suggest us to rewrite (27) exploiting a first-order accurate backward formula for the time derivative. It can be shown that one gets

$$\mathbf{v}^{*} = \bar{\mathbf{v}}^{n+1} + \Delta t \left\{ \underline{\nabla}\phi_{\mathrm{AB}}^{n} + \left[I - \frac{\Delta t}{2} \underline{\nabla} \cdot (2\nu \underline{\nabla}^{s}) \right] (\underline{\nabla}\phi_{\mathrm{AB}}^{n} - \underline{\nabla}\phi_{\mathrm{AB}}^{n-1}) \right\} + O(\Delta t^3) \tag{32}$$

Therefore, by defining $\Delta t(\underline{\nabla}\phi_{\mathrm{AB}}^{n} - \underline{\nabla}\phi_{\mathrm{AB}}^{n-1}) \equiv \underline{\nabla}\Phi$, the congruent boundary condition for Equation (13) is

$$\boxed{\mathbf{v}_{\partial}^{*} = f_{\mathrm{AB}} = \bar{\mathbf{v}}_{\partial}^{n+1} + \Delta t \underline{\nabla}\phi_{\mathrm{AB}}^{n}|_{\partial} + \left[I - \frac{\Delta t}{2} \underline{\nabla} \cdot (2\nu \underline{\nabla}^{s}) \right]\Big|_{\partial} \underline{\nabla}\Phi + O(\Delta t^3)} \tag{33}$$

The attractive feature of Equation (33) is that it is very simple to be implemented and clearly expresses the meaning of the additional terms necessary for obtaining congruent intermediate boundary conditions in LES approaches. Indeed, the term $\underline{\nabla}\Phi$ takes into account the time evolution of the auxiliary gradient field along the boundaries. This feature is the main key to avoid the problems addressed in Section 4.1, in points (a) and (b). Observe that only the time-regularity of the real filtered pressure gradient was required whereas the auxiliary gradient fields have been used only in discrete sense, according to their true meaning in the fractional step method. Of course, provided that the velocity field is the unfiltered one, Equation (33) is adoptable also for performing a DNS with the PFP method. Indeed, the auxiliary gradient field intrinsically adapts itself to the adopted velocity.

Some analytical test-cases should be adopted to achieve the quantitative analysis of the performances of (33). As a matter of fact this is not a straightforward task in case of LES computations. Thus only a specific numerical test-case for confined flows will be used in the following for testing the efficiency of (33).

For the sake of completeness, let us highlight that this paper follows and integrates the studies published in References [10, 11] where a theoretical analysis of the local truncation error, as well as of the correct intermediate boundary conditions for the PFP method, was addressed for simulations of laminar flows. Furthermore, the new expression of the intermediate boundary condition has been preliminarily adopted for performing a simulation of a 2D time-evolving mixing layer [27]. These papers should be considered for getting a more comprehensive framework of the issues herein addressed.

5. NUMERICAL RESULTS

The problem adopted for the tests is constituted by a confined three-dimensional flow in a channel having the Cartesian stream-wise flow direction x, the span-wise z and the vertical y. The geometry of the channel is specified by fixing the height $L_y = H$, the stream-wise length $L_x = \frac{3}{2}\pi L_y$ and the span-wise one $L_z = \frac{1}{2}\pi L_y$. The reference length is chosen as $L_{\mathrm{r}} = H$, thus the non-dimensional geometry parameters (indicated in the following with the superscript $\times$)

are $L_y^\times = 1$, $L_x^\times = 3\pi/2$, $L_z^\times = \pi/2$. The results obtained for steady and forced periodic channel flow as well as for a channel flow with inflow/outflow are illustrated in the following sections.

5.1. Periodic channel flows

In this case, the problem has two homogeneous flow directions along x,z coordinates, respectively. Therefore, periodic boundary conditions are adopted in x and z directions, while no slip conditions act in y direction at the upper and lower walls. Let us highlight an important issue about this test. Although such a problem is widely adopted as test-case, it is not fully indicative of the real performance of a projection method. This happens as the Helmholtz–Hodge decomposition is guaranteed to be purely orthogonal when such boundary conditions are in effect [8, 11, 15]. Thus, the numerical boundary layer mode on the auxiliary gradient field is orthogonal to the velocity one. Hence, by using this flow problem, one should be aware of such a peculiarity in the accuracy analysis.

The tests are performed both in DNS and in LES approaches and they are subdivided in two sub-cases, the first with a base pressure gradient constant in time, the second with a time-varying forcing one (pulsating channel flow) according to Reference [28]. Although this paper focuses on LES accuracy, comparisons between DNS cases are also useful since they mainly highlight the effect of the accuracy of the tangential velocity components obtainable with the HHD principle, without mixing also the interference of the SGS modelling. LES results are then also compared each other for clarifying the differences in the solutions.

Concerning the DNS equations (1) and (2), the pressure in the channel is subdivided into three contributions, that are $p' = (1/\rho_0)(p + p_\mathrm{b} + p_\mathrm{o})$, wherein $p = p(\mathbf{x}, t)$ is the *residual* pressure required to enforce continuity, $p_\mathrm{b} = p_\mathrm{b}(x)$ the *base* pressure driving the average flow along the stream-wise direction x and $p_\mathrm{o} = p_\mathrm{o}(x, t)$ the superimposed *oscillating* pressure.

Of course, the base pressure must satisfy the relation $p_\mathrm{b}(x) = p_0 + (\rho_0 \nu C)x$, being C a constant corresponding to the second derivative along y of the average stream-wise velocity. For a channel of stream-wise periodic length L_x one has $C = (p_\mathrm{b}(L_x) - p_0)/(\rho_0 \nu L_x) = \Delta p_0/(\rho_0 \nu L_x)$ therefore, $p_\mathrm{b}(x) = p_0 + \Delta p_0 x/L_x$ and the constant p_0 can be arbitrarily set to zero.

Then, for a pressure oscillating to a frequency $\omega = 2\pi/T$, being T the characteristic period, one has $p_\mathrm{o}(x, t) = [\Delta p_0 \alpha \cos(\omega t)]x/L_x$ where α is a non-dimensional value. Hence, the total pressure gradient rewrites as

$$\underline{\nabla} p' = \frac{1}{\rho_0} \underline{\nabla} p + \mathbf{i} \frac{\Delta p_0}{\rho_0 L_x} [1 + \alpha \cos(\omega t)] \tag{34}$$

where $\mathbf{i}$ is the unit vector along the x direction.

Now, the reference velocity V_r is chosen as $\mathbf{v} = V_\mathrm{r} \mathbf{v}^\times$, the reference time as $t_\mathrm{r} = H/V_\mathrm{r}$, the reference pressure as $p_\mathrm{r} = \rho_0 V_\mathrm{r}^2$, so that the unfiltered NS equations (1), (2) are rewritten in non-dimensional form as

$$\underline{\nabla}^\times \cdot \mathbf{v}^\times = 0 \tag{35}$$

$$\frac{\partial \mathbf{v}^\times}{\partial t^\times} + \underline{\nabla}^\times \cdot (\mathbf{v}^\times \mathbf{v}^\times) + \underline{\nabla}^\times p^\times + \mathbf{i}[1 + \alpha \cos(Re_\tau \omega^\times t^\times)] = \frac{1}{Re_\tau} \nabla^{2^\times} \mathbf{v}^\times \tag{36}$$

where $Re_\tau = u_\tau H/\nu$ is the Reynolds number with $u_\tau \equiv V_r = \sqrt{(\Delta p_0 H)/(\rho_0 L_x)}$ where the mean friction velocity u_τ has been chosen as reference velocity. The reference forcing frequency in wall units is $\omega_r = u_\tau^2/\nu$ therefore, it is sufficient to set $\alpha = 0$ in (36) to switch from pulsating to steady channel flow.

On the other hand, concerning the LES equations (4) and (7), the filtered pressure in the channel is $\bar{\pi} = (1/\rho_0)(\bar{p} + \overline{p_b} + \overline{p_o}) + \frac{1}{3}\,\mathrm{Tr}(\bar{\mathbf{T}})$ thus, the total pressure gradient rewrites as

$$\begin{aligned}\underline{\nabla}\bar{\pi} &= \frac{1}{\rho_0}(\underline{\nabla}\bar{p} + \underline{\nabla}\overline{p_b} + \underline{\nabla}\overline{p_o}) + \frac{1}{3}\underline{\nabla}\,\mathrm{Tr}(\bar{\mathbf{T}}) \\ &= \frac{1}{\rho_0}\underline{\nabla}\bar{p} + \mathbf{i}\frac{\Delta p_0}{\rho_0 L_x}[1 + \alpha\,\cos(\omega t)] + \frac{1}{3}\underline{\nabla}\,\mathrm{Tr}(\bar{\mathbf{T}}) \\ &= \frac{1}{\rho_0}\underline{\nabla}\Pi + \mathbf{i}\frac{\Delta p_0}{\rho_0 L_x}[1 + \alpha\,\cos(\omega t)] \end{aligned} \tag{37}$$

having defined $(1/\rho_0)\underline{\nabla}\Pi \equiv (1/\rho_0)\underline{\nabla}\bar{p} + \frac{1}{3}\underline{\nabla}\,\mathrm{Tr}(\bar{\mathbf{T}})$. Now, by properly setting $\pi_r = \rho_0 u_\tau^2$, since the Smagorinsky model expresses $\nu_{\mathrm{LES}} = (C\Delta)^2|\bar{\mathbf{D}}| = u_\tau H (C\Delta^\times)^2 |\bar{\mathbf{D}}^\times|$, the filtered NS equations (4), (7) are rewritten in non-dimensional form as

$$\underline{\nabla}^\times \cdot \bar{\mathbf{v}}^\times = 0 \tag{38}$$

$$\frac{\partial \bar{\mathbf{v}}^\times}{\partial t^\times} + \underline{\nabla}^\times \cdot \overline{\bar{\mathbf{v}}^\times \bar{\mathbf{v}}^\times} + \underline{\nabla}^\times \Pi^\times + \mathbf{i}[1 + \alpha\,\cos(Re_\tau \omega^\times t^\times)] = \underline{\nabla}^\times \cdot \left[2\left(\frac{1}{Re_\tau} + \nu_{\mathrm{LES}}^\times\right)\bar{\mathbf{D}}^\times\right] \tag{39}$$

wherein $\nu_{\mathrm{LES}}^\times = \nu_{\mathrm{LES}}/u_\tau H = (C\Delta^\times)^2 |\bar{\mathbf{D}}^\times|$. Furthermore, the Van Driest damping function [1] is added to tune the eddy viscosity intensity close to the walls.

In order for analysing the results, one of the controlled quantities is the stress on the walls, which is $\tau_w(x,z,t) = \mu(\partial u/\partial y)|_{y_w},\ y_w = 0, 1$. Hence, the non-dimensional stress becomes

$$\tau_w^\times(x^\times, z^\times, t^\times) = \mu\frac{u_\tau}{\tau_r H}\left.\frac{\partial u^\times}{\partial y^\times}\right|_{y_w^\times} = \left.\frac{1}{Re_\tau}\frac{\partial u^\times}{\partial y^\times}\right|_{y_w^\times} \tag{40}$$

having chosen the reference stress $\tau_r = \pi_r = \rho_0 u_\tau^2$. In case of LES, the meaning of Equation (40) extends to the normal derivative of the filtered x velocity component, that is $\bar{u}^\times$.

The numerical results will be also post-processed by means of some averaging operators. A first data reduction is obtained by performing on a quantity $f(x^\times, y^\times, z^\times, t^\times)$ (DNS or LES variable) the average over the z direction (indicated by the symbol $\bar{f}^z$) and the time (indicated by the symbol $\langle f \rangle$) according to

$$\langle \bar{f}^z \rangle (x^\times, y^\times) = \frac{1}{T_p L_z^\times}\int_{t_0}^{t_0+T_p} \mathrm{d}\tau \int_0^{L_z^\times} f(x^\times, y^\times, \zeta, \tau)\,\mathrm{d}\zeta \tag{41}$$

where t_0 is a suitable initial time of integration and T_p the total integration time. The initial time t_0 is suitably chosen by controlling the full development of the time evolution of the

variables as well as of the rms quantities. More specifically, the function f in (41) will be a velocity component among $u^\times, v^\times, w^\times$, for DNS, or $\bar{u}^\times, \bar{v}^\times, \bar{w}^\times$, for LES approaches, respectively.

Thus, some results are provided in terms of the one-dimensional energy spectra

$$E_{ss}(k) = \frac{1}{L_y^\times} \int_0^{L_y^\times} |\hat{C}(k,\eta)|^2 \, \mathrm{d}\eta \tag{42}$$

for $s = \langle \overline{u^\times}^z \rangle, \langle \overline{v^\times}^z \rangle, \langle \overline{w^\times}^z \rangle$ in case of DNS or $s = \langle \overline{\bar{u}^\times}^z \rangle, \langle \overline{\bar{v}^\times}^z \rangle, \langle \overline{\bar{w}^\times}^z \rangle$ in case of LES variables, having indicated with $\hat{C}(k,\eta)$ the complex coefficients of the 1-D Fourier transform along the x direction, i.e. $\langle \bar{f}^z \rangle(x^\times) = \sum_q \hat{C}(k) \mathrm{e}^{\mathrm{i}kx^\times}$ with $k = 2\pi q / L_x^\times$ and q the wavenumber.

Moreover, stresses (40) are controlled in time according to the average

$$\overline{\tau_w^\times}^{x,z}(t^\times) \triangleq \frac{1}{L_x^\times L_z^\times} \int_0^{L_x^\times} \mathrm{d}\xi \int_0^{L_z^\times} \tau_w^\times(\xi, \zeta, t^\times) \, \mathrm{d}\zeta \tag{43}$$

as well as they are also reduced along x according to this other average

$$\langle \overline{\tau_w^\times}^z \rangle(x^\times) = \frac{1}{T_p L_z^\times} \int_{t_0}^{t_0+T_p} \mathrm{d}\tau \int_0^{L_z^\times} \tau_w^\times(x^\times, \zeta, \tau) \, \mathrm{d}\zeta \tag{44}$$

from which the results are then provided in terms of the one-dimensional energy spectrum

$$E_{\tau_w}(k) = |\hat{\tau}_w(k)|^2 \tag{45}$$

Then, the rms velocity fluctuations are considered. Specifically, the fluctuation f' is herein defined as the residual around the function $\langle \bar{f}^{x,z} \rangle(y^\times)$ according to

$$\langle \bar{f}^z \rangle(x^\times, y^\times) - \langle \bar{f}^{x,z} \rangle(y^\times) \triangleq f'(x^\times, y^\times) \tag{46}$$

so that the rms of the fluctuation is

$$\mathrm{RMS}_{f'}(y^\times) \triangleq \left(\frac{1}{L_x^\times} \int_0^{L_x^\times} f'^2 \, \mathrm{d}\xi \right)^{1/2} \tag{47}$$

Let us remind that the goal of this study is to analyse the numerical methodology for LES and to test the performances of the different boundary conditions but is not intended for providing new insights into the physical flow structure of channel flows. Therefore, a classical second-order finite volume discretization has been adopted, as it was already tested in the studies [10, 11]. More specifically, the CN integration is adopted only for the vertical y-component of the molecular diffusive term. Accordingly, a moderate Reynolds number is used and commutation terms between non-uniform filter and derivatives are disregarded. However, more sophisticated and accurate schemes are currently developed, i.e. a deconvolution-based finite volume fourth-order centred discretization on non-uniform grids [27] and fifth-order upwind ones [29].

All the following results are obtained for $Re_\tau = 70$ while by fixing the forcing parameters $\alpha = 1$, $\omega^\times = 0.1$, the pulsating channel flow is onset. Setting a random divergence-free velocity field as initial condition the simulations are started, hence, the numerical solution develops and correlates then, after the numerical transient is finished, the time average is started.

Concerning the grid resolution, stream-wise and span-wise directions are discretized with a uniform grid whereas a non-uniform grid (by means of a cosine-law stretching) is adopted in the normal walls direction.

The adopted DNS grid has $70 \times 25 \times 35$ cells, allowing to get the grid size measures $\Delta x^+ \approx 4.7$, $\Delta z^+ \approx 3.1$ (the superscript '+' expresses a length in wall units, i.e. $\Delta x^+ = u_\tau \Delta x/\nu = Re_\tau \Delta x^\times$, $\Delta z^+ = u_\tau \Delta z/\nu = Re_\tau \Delta z^\times$) and the first point in the boundary layer is located at $y^+ \approx 0.14$.

The adopted LES grid has $35 \times 16 \times 20$ cells allowing us to get the grid size measures $\Delta x^+ \approx 9.4$, $\Delta z^+ \approx 5.5$ and the first point in the boundary layer is located at $y^+ \approx 0.34$. The Smagorinsky constant is fixed to $C = 0.2$ and $\Delta^\times = 2(\Delta x^\times \Delta z^\times)^{1/2}$. In order to test the behaviour of the intermediate boundary conditions, the simulations are carried out for three different time-steps, i.e. $\Delta t = 0.001,\ 0.0005, 0.00025$. It is worthwhile highlighting that the tests are not performed at constant Courant number therefore, for vanishing time-step, there would be the appearance of a constant local truncation error term which is proportional to the square of the spatial mesh sizes, see the analysis in References [10, 11].

For the DNS, after controlling the numerical transient and the rms quantities, the non-dimensional time for starting the average is chosen as $t_0 = 62.5$ and the period of integration is $T_{p\_\mathrm{DNS}} = 25$ while, for the LES, the non-dimensional time for starting the average is chosen as $t_0 = 200$ and the period of integration is $T_{p\_\mathrm{LES}} = 100$.

The following sub-sections illustrate the results for each one of the flow cases. The figures reporting the energy spectra are drawn in a double logarithmic scale whereas the wavenumber value is normalized by a general zero wavenumber $k_0 = 2\pi/P$. Thus, k_0 is representative a longitudinal wavenumber and, both for DNS and LES simulations, the longitudinal periodic length is the same $P = L_x^\times = 3\pi/2$.

5.1.1. Steady channel flow. Direct numerical simulations: In Figures 2–4 are reported the DNS results in terms of the stream-wise one-dimensional energy spectra for the three velocity components (42), the rms of the velocity fluctuation (47) and the stream-wise one-dimensional energy spectra of wall stresses (44), respectively. Moreover, in each figure, left ((a), (c), (e)) and right ((b), (d), (f)) columns illustrate the computations performed for the three time-steps with first- and second-order intermediate boundary conditions, respectively.

Specifically, the energy spectra shown in Figure 2 are descriptive of the fact that an almost time-step-independent solution (especially at high wavenumbers) is reached when boundary conditions (33) are used whereas stronger oscillations appear in the solutions, obtained with (16), from (a) to (e) especially at low and medium wavenumbers. This feature is an indication that the contribute of the local truncation error, that depends on the time-step, reduces more rapidly using the second-order intermediate boundary conditions, similarly to the appearances reported in References [10, 11] for an analytical solution, while a monotonic reduction seems still not reached with the first-order ones. By looking to the pictures, two main peaks, corresponding to the appearance of coherent eddy structures formed in the flow, are always individuated at practically the same wavenumbers for all figures but magnitude are different.

The Figure 3 is much more explicative of such features. In fact, the rms velocity fluctuations along the vertical direction enhance the differences in the two methods, particularly comparing the results at the smallest time-step, i.e. figures (e)–(f). Although some lack in the symmetry of the rms profiles can be adduced to the fact that $T_{p\_\mathrm{DNS}} = 25$ is a rather small time interval, anyway the differences in the peaks are relevant and no longer depending on the time average.

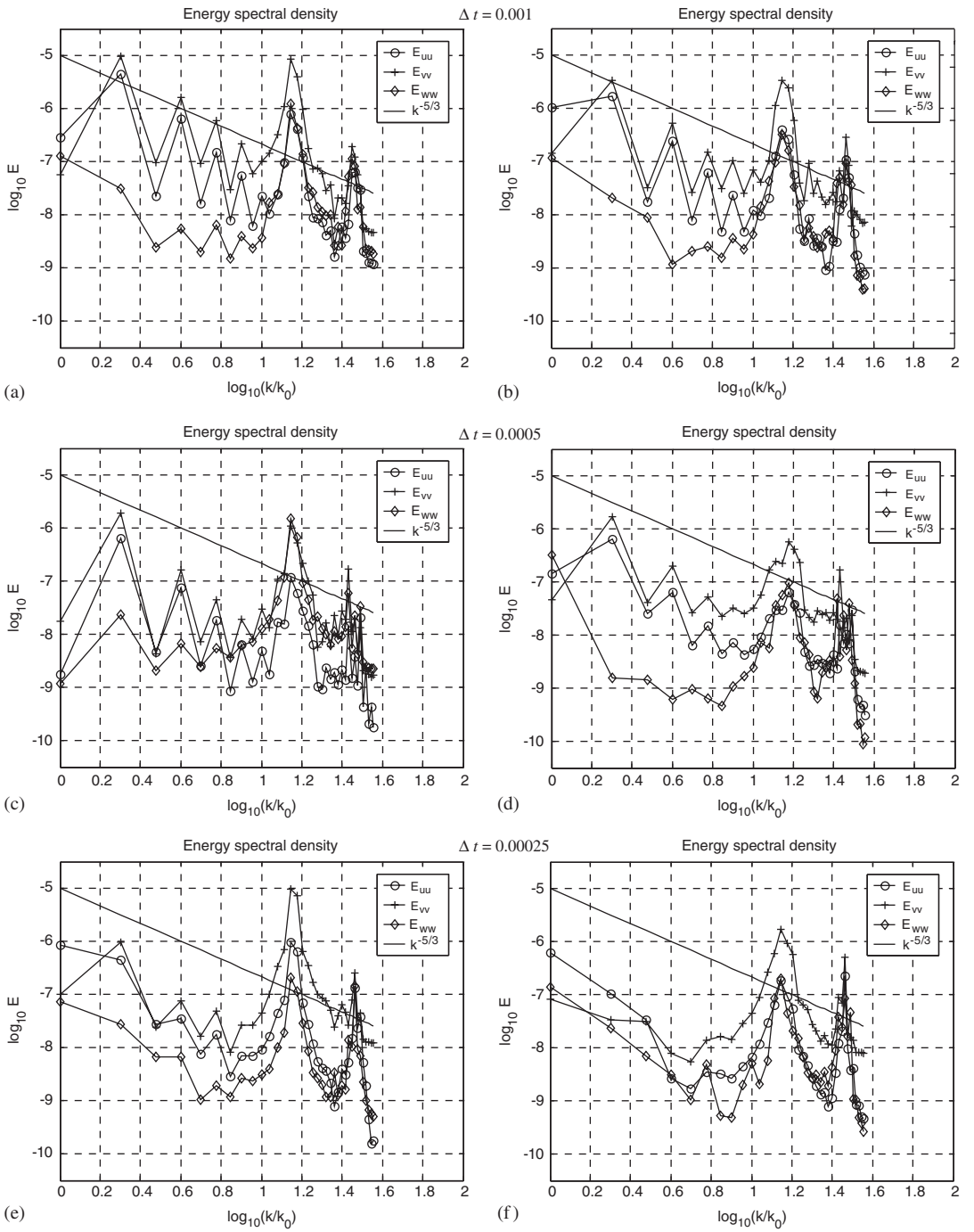

Figure 2. DNS of the steady channel flow. Stream-wise one-dimensional energy spectra for the velocity components. Intermediate boundary conditions (16) (left column) and (33) (right column).

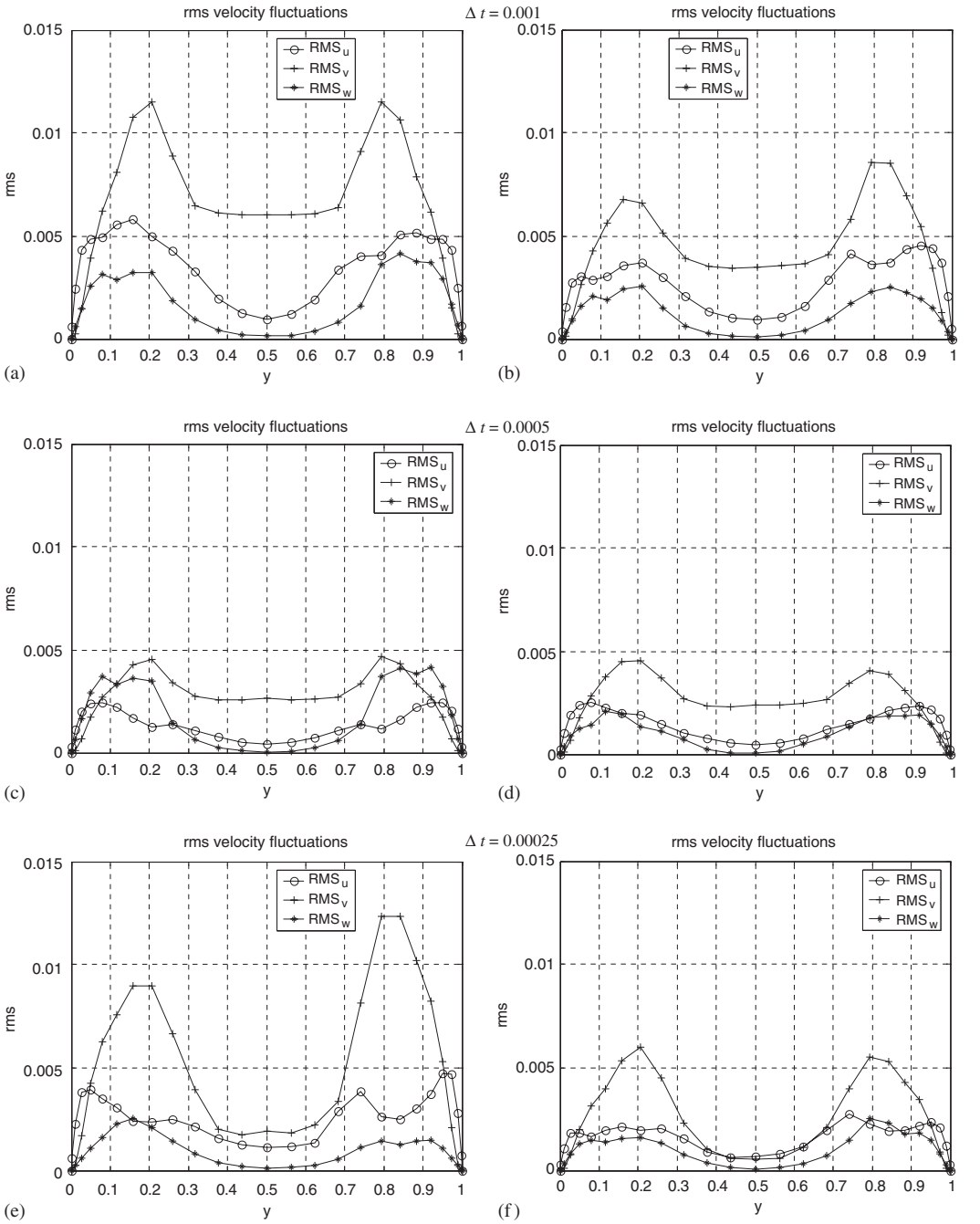

Figure 3. DNS of the steady channel flow. RMS velocity fluctuations. Intermediate boundary conditions (16) (left column) and (33) (right column).

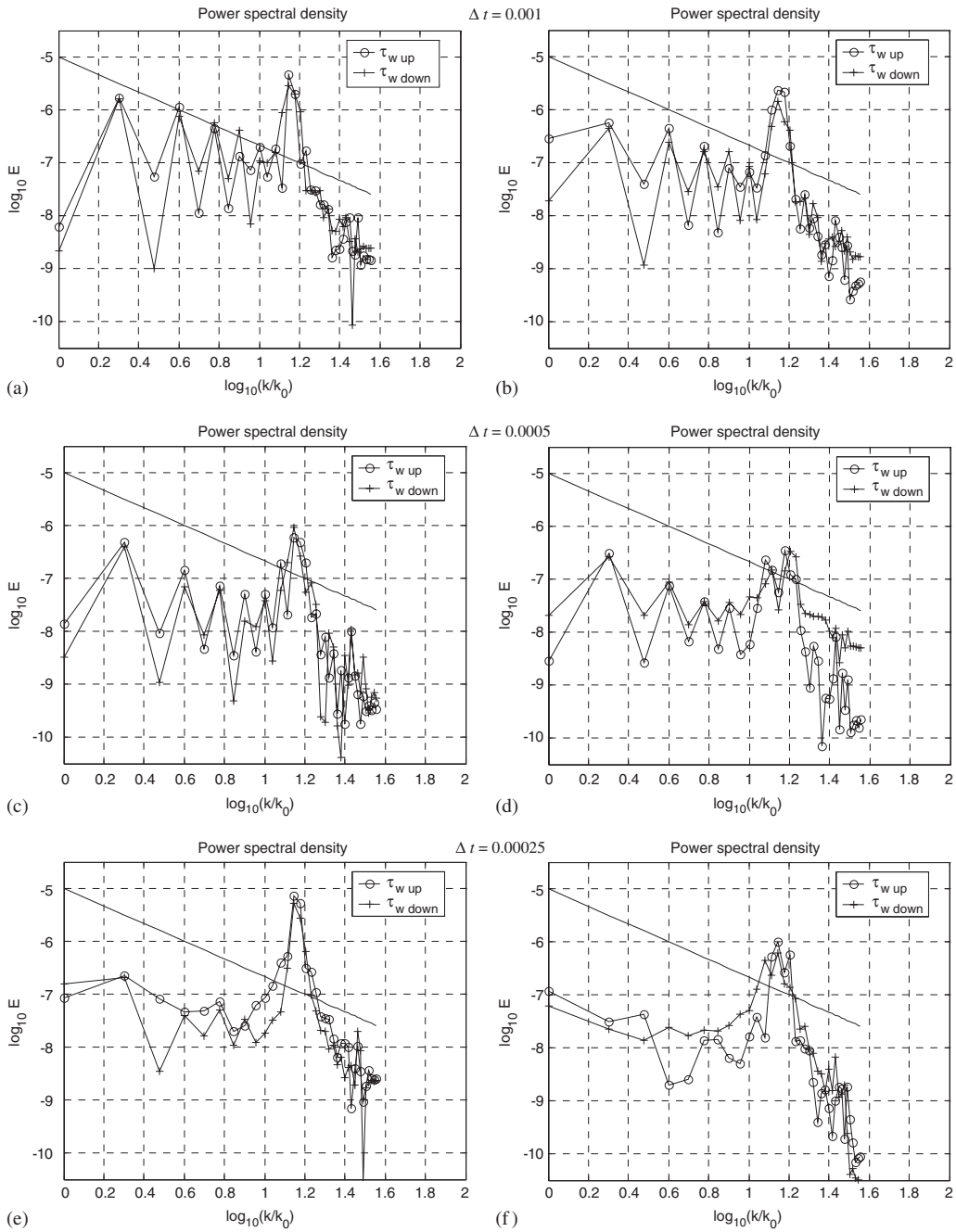

Figure 4. DNS of the steady channel flow. Stream-wise one-dimensional energy spectra for the stresses on the upper (up) and lower (down) walls. Intermediate boundary conditions (16) (left column) and (33) (right column).

It is very interesting to see that the three rms practically vanish far from the walls only when second-order intermediate boundary conditions are used (let us remind that the central value $y=0.5$ corresponds to $y^+=35$ and the two RMS_v peaks in figure (e) at $y=0.2$ and $y=0.8$ correspond to $y^+=14$) indicating that the solution has reached a good accuracy.

Figure 4 shows again that the results obtained with (33) are more time-step independent, differently from those obtained with (16). Let us observe that, at this moderate Reynolds number, the appearance in the spectra of an inertial sub-range region is rather limited and however, owing to the flow anisotropy, not fully justified near the wall.

Large eddy simulations: Next, the LES results are illustrated in Figures 5–7, organized in the same way as it was previously reported for DNS. Let us remark that it is well assessed that LES simulations of channel flows with the static SGS eddy–viscosity model are generally too dissipative and the dynamic procedure is preferable. However, in the present paper the results obtained with the dynamic procedure are not reported because the action of the dynamic SGS modelling would make more complex to discern the main differences and recognize the reasons. Actually, the goal of the present simulations is to test the dependence of the results on the adopted intermediate boundary conditions while fixing all the other computation parameters, including the SGS parameters. Now, having the DNS solutions in mind, the LES results can be both compared each other and compared with DNS.[‖] Let us highlight that the cut-off wavenumber due to the grid resolution along x (Nyquist frequency $k_{\max}=\pi/\Delta x$) is $\log_{10}(k_{\max}/k_0)\approx 1.3$ but the use of the top-hat filter (i.e. a smooth filter) affects the energy content also before it, that is in the higher part of the resolved wavenumber range. This is the reason that motivated us to using the deconvolution approach [27, 29] but, for the sake of simplicity, this approach is not added in the present LES method.

The energy spectra in Figure 5(a), (c), (e), indicate again that the first-order intermediate boundary conditions (16) produce strong oscillations whereas the spectra obtained with (33) show a slower variation. However, both methods produce an energy content at low wave-numbers that is greater than that obtained with the DNS methods (observe that although the log scales in DNS and LES plots are with different extremes, the continuous line indicating the inertial scaling is posed at the same level, helping in comparisons), very probably owing to aliases errors introduced by the second-order discretization. Moreover, the two columns indicate that the energy levels of u and v velocity components interchange each other at the smallest time-step, see figures (e) and (f), according to the DNS results that showed a greater energy level of the vertical velocity. It is worthwhile noticing that figures (e) and (f) clearly show that the first-order intermediate boundary conditions produce a stronger dissipation of the energy content than second-order one. Although there is a heavy effect of static eddy viscosity model, the differences are also caused by the fact that the numerical boundary layer produced by (16) added dissipation to that introduced by the SGS modelling while (33) is able to reduce this effect. However, owing to the dissipation near the cut-off, no one of the energy peaks present in DNS is clearly highlighted in both LES methods.

Figure 6 shows the rms velocity fluctuations for LES as defined in Equations (46), (47) applied on the filtered velocities. Again, at the smallest time-step, see figures (e) and (f), the differences in terms of the peaks magnitude are rather pronounced. Symmetry is obtained

[‖] In principle, the comparison would require to filter the DNS solution at each time-step and make the statistic over the filtered data. Here, this procedure is not performed and unfiltered DNS results are used.

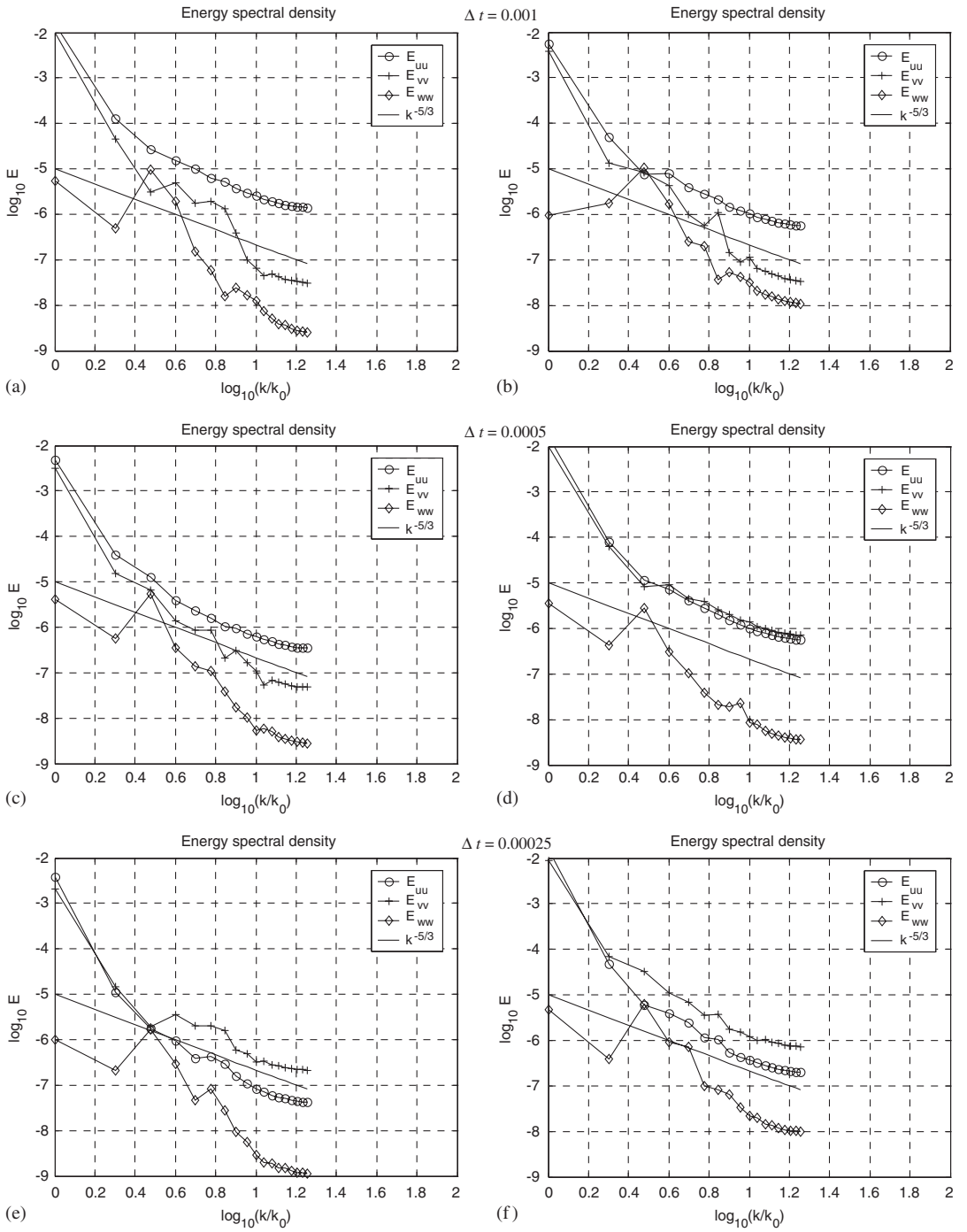

Figure 5. LES of the steady channel flow. Stream-wise one-dimensional energy spectra for the velocity components. Intermediate boundary conditions (16) (left column) and (33) (right column).

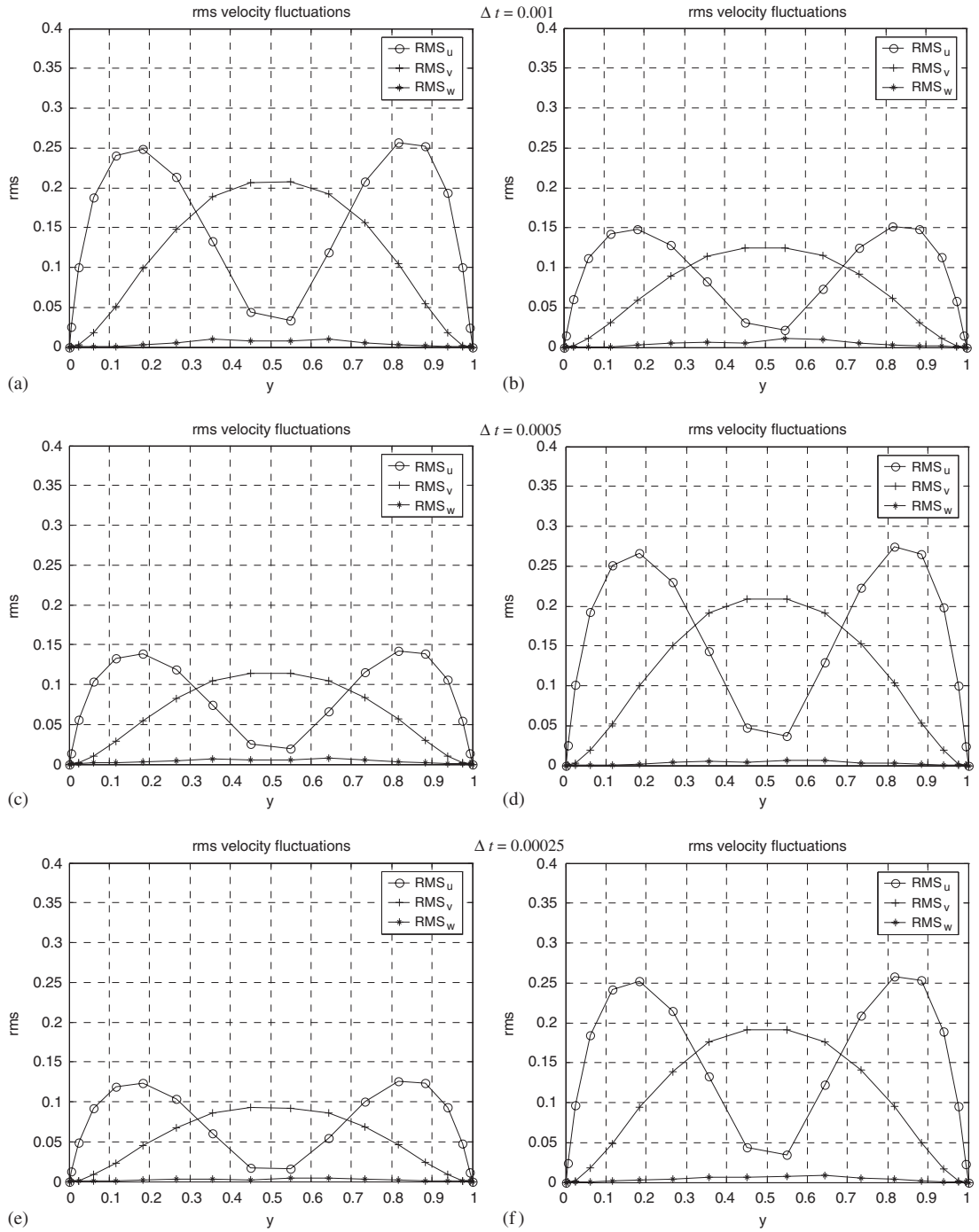

Figure 6. LES of the steady channel flow. RMS velocity fluctuations. Intermediate boundary conditions (16) (left column) and (33) (right column).

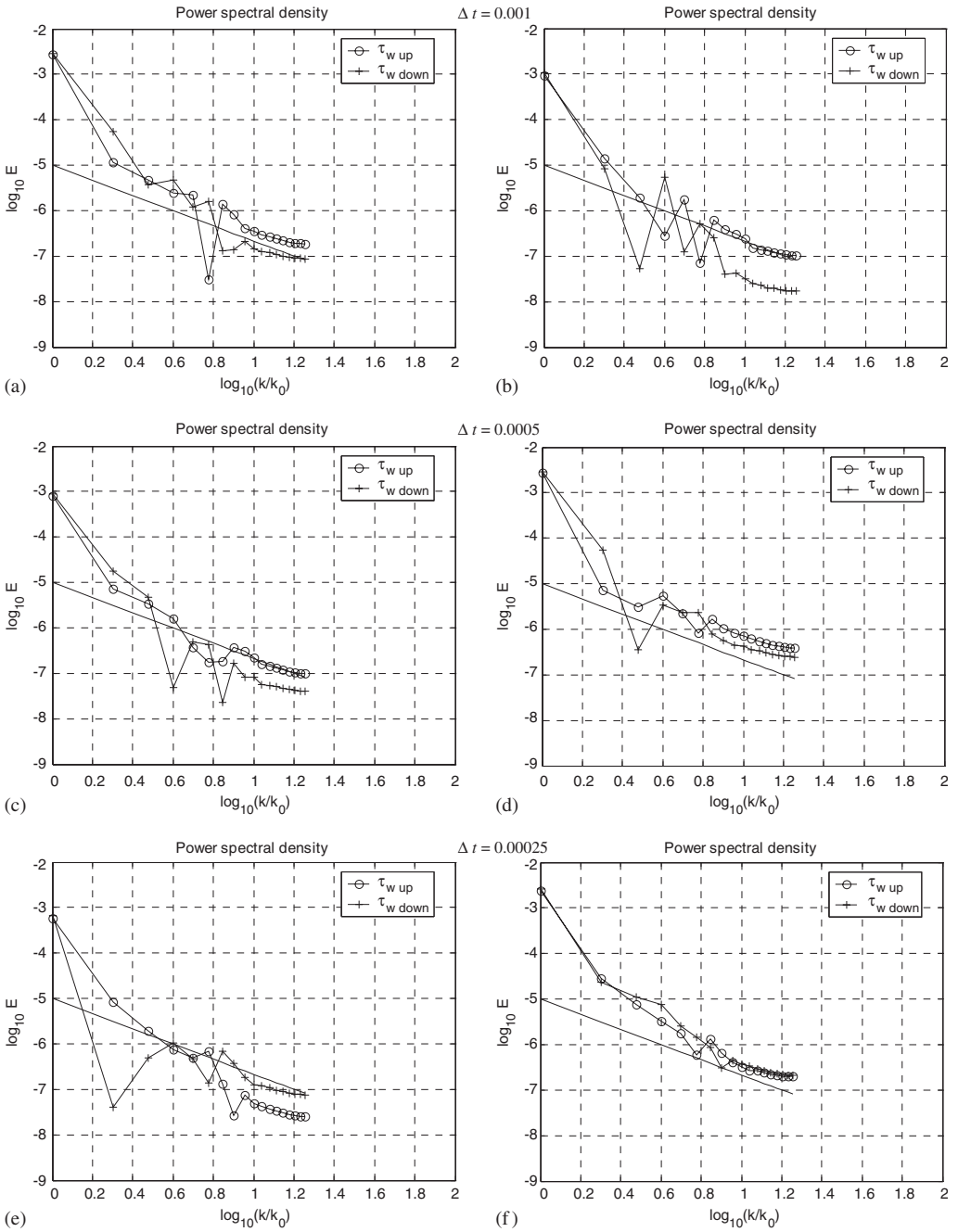

Figure 7. LES of the steady channel flow. Stream-wise one-dimensional energy spectra for the stresses on the upper (up) and lower (down) walls. Intermediate boundary conditions (16) (left column) and (33) (right column).

in all simulations, confirming that $T_{p\_\mathrm{LES}} = 100$ is sufficient. However, it is evident that the behaviour individuated in the two columns is different: in the left one the peaks magnitude reduces for diminishing time-step while in the right one the peaks magnitude increases.

Figure 7 illustrates the one-dimensional energy content of the wall stresses (44) and is very representative of the convergence behaviour of the two methods. From figures (a) to (e) compared to (b) to (f) is evident that (16) did not allow us to reach a time-step independent solution, up at the smallest time-step, presenting several oscillations, whereas (33) allows us to get a sufficiently smooth spectra, see (e) and (f) for comparison. Particularly evident is the fact that the upper and lower stresses have the same energy content only in figure (f) whereas figure (e) shows a greater dissipation.

5.1.2. Pulsating channel flow. The pulsating channel flow is now tested because the unsteady mean pressure gradient forces the velocities to be excited at some wavenumber thus resulting a more critical test-case for checking the time accuracy of the intermediate boundary conditions. The aim is to confirm the advantage of (33), especially in computing the quantities near the walls. Similar to the organization of the previous sub-section, the results are reported for three time-steps and the intermediate boundary conditions (16) and (33) are indicated in the left and right columns, respectively. The figures are reported first for DNS (Figures 8–10) then for LES (Figures 11–13).

Direct numerical simulations: Concerning DNS results, Figure 8 shows the one-dimensional energy spectra of the three velocity components. Now, differently from the steady flow channel, it appears a peak in all the spectra at $\log_{10}(\bar{k}/k_0) = 0.6$ as a response to the pulsating frequency $\omega^{\times} = 0.1$. However, figure (a) shows a peak also at lower wavenumber, caused by the lower accuracy of (16) coupled with aliasing errors. Decreasing the time-step, such a peak disappears in (c) and (e) but the global behaviour appears confirming the oscillations already reported in the results for the steady case. Furthermore, it appears that, by using (16), the energy content at low wavenumbers is systematically lower than that obtained by using (33). What is more, also the highest wavenumbers of the spectra highlight a stronger dissipation; indeed, comparing (e) and (f) it appears that the energy peaks in (f), close to the cut-off, are no longer present with first-order boundary conditions (16).

The rms fluctuations, illustrated in Figure 9, confirm the previous features. It is interesting to see that for the higher time-step, see figure (a), the results obtained with (16) are self-explicative of the effect of the lack of accuracy. In general, from figures (a), (c), and (e) it seems that the rms have not reached a time-step independent solution. By comparing figures (e) and (f) one sees the difference in the vertical velocity. The energy content of the walls stresses is reported in Figure 10. The behaviours are quite similar to what already addressed concerning Figures 8. Particularly, comparing (e) and (f), it can be observed a greater dissipation of the energy content at highest wavenumber when (16) is used.

Large eddy simulations: Again, the LES results are compared each other for the two methods and with the DNS results previously illustrated (again the reference is the continuous line of the ideal slope). The energy spectra reported in Figure 11(a), 11(c) and 11(e) shows the fact that the solution is still not time-independent at the smallest time-step whereas (b), (d) and (f) are rather similar. It is not sufficiently evident a specific energy peak corresponding to a response to the pulsating frequency and this fact has to be adduced to the strong dissipation of the static SGS model. However, from comparison of figure (e) and (f), it appears that the energy content, especially at high wavenumber, is greatly dissipated with the intermediate

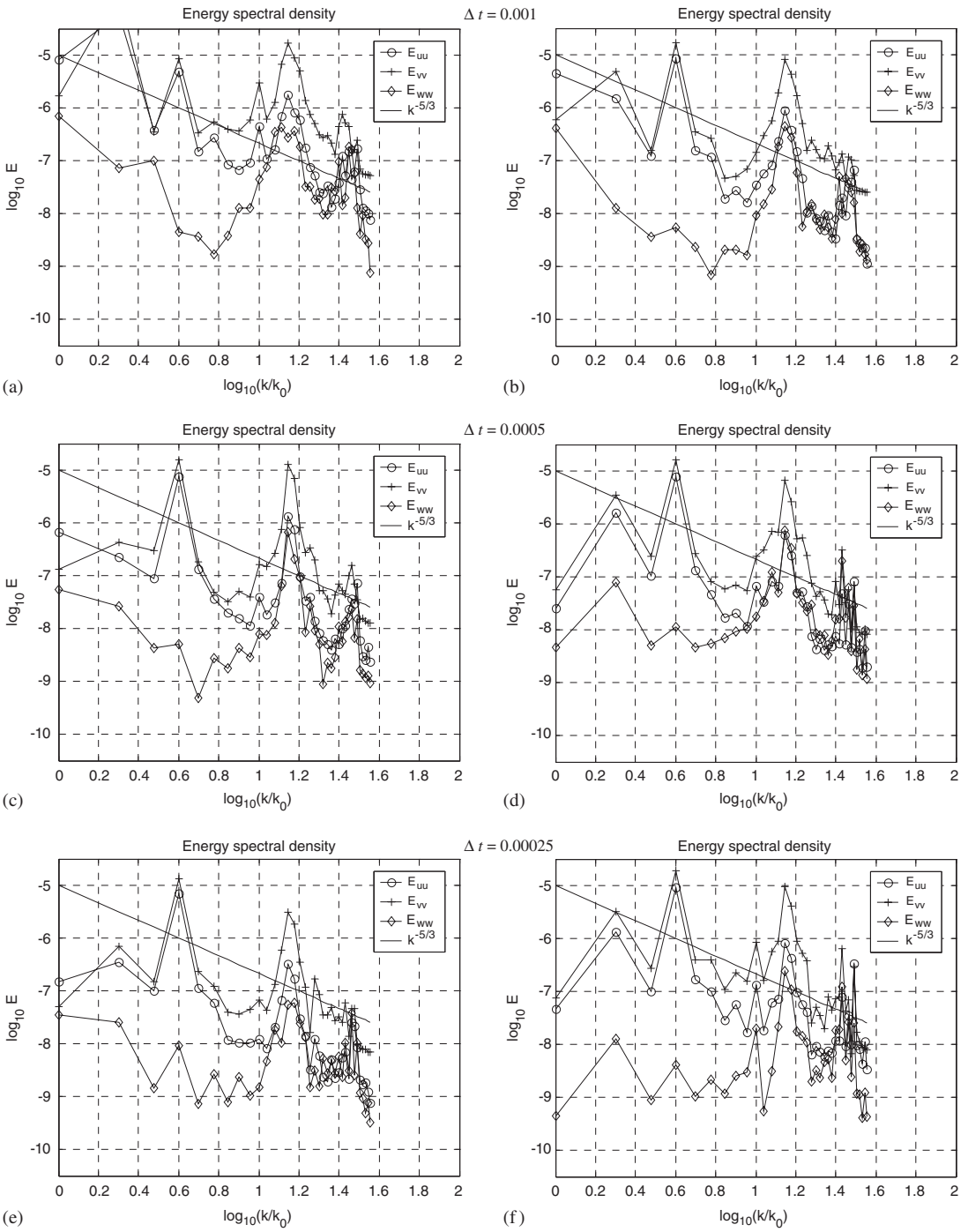

Figure 8. DNS of the pulsating channel flow. Stream-wise one-dimensional energy spectra for the velocity components. Intermediate boundary conditions (16) (left column) and (33) (right column).

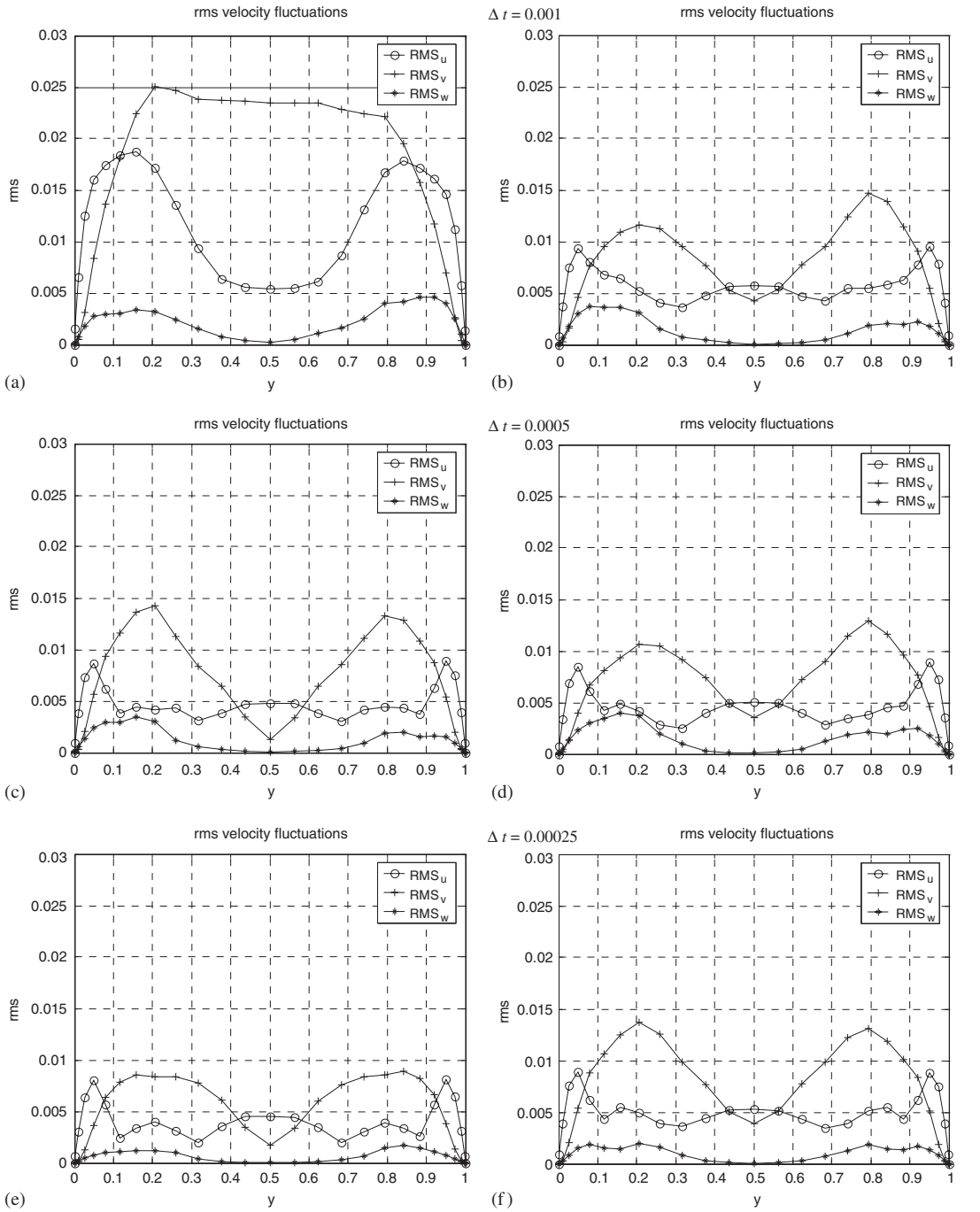

Figure 9. DNS of the pulsating channel flow. RMS velocity fluctuations. Intermediate boundary conditions (16) (left column) and (33) (right column).

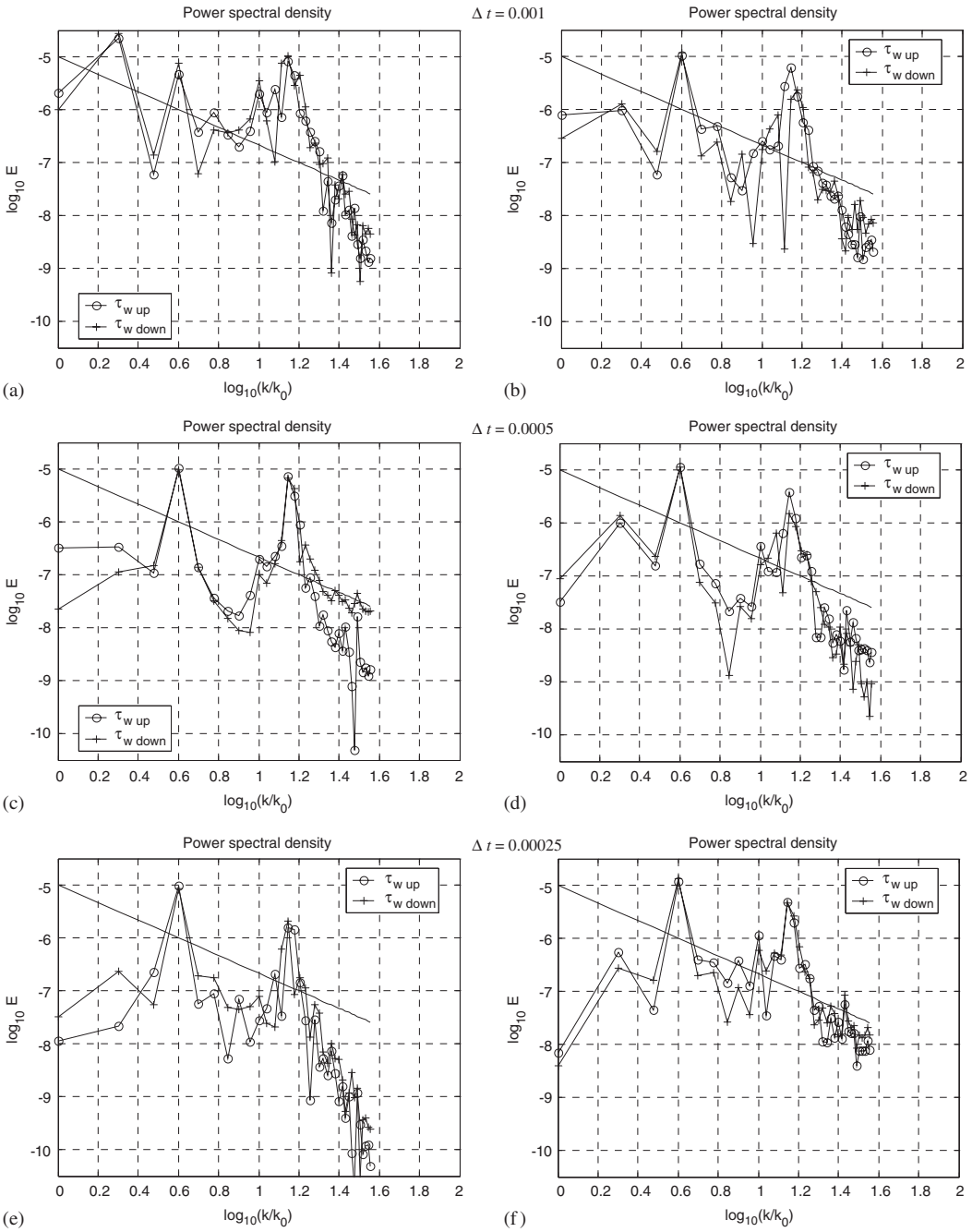

Figure 10. DNS of the pulsating channel flow. Stream-wise one-dimensional energy spectra for the stresses on the upper (up) and lower (down) walls. Intermediate boundary conditions (16) (left column) and (33) (right column).

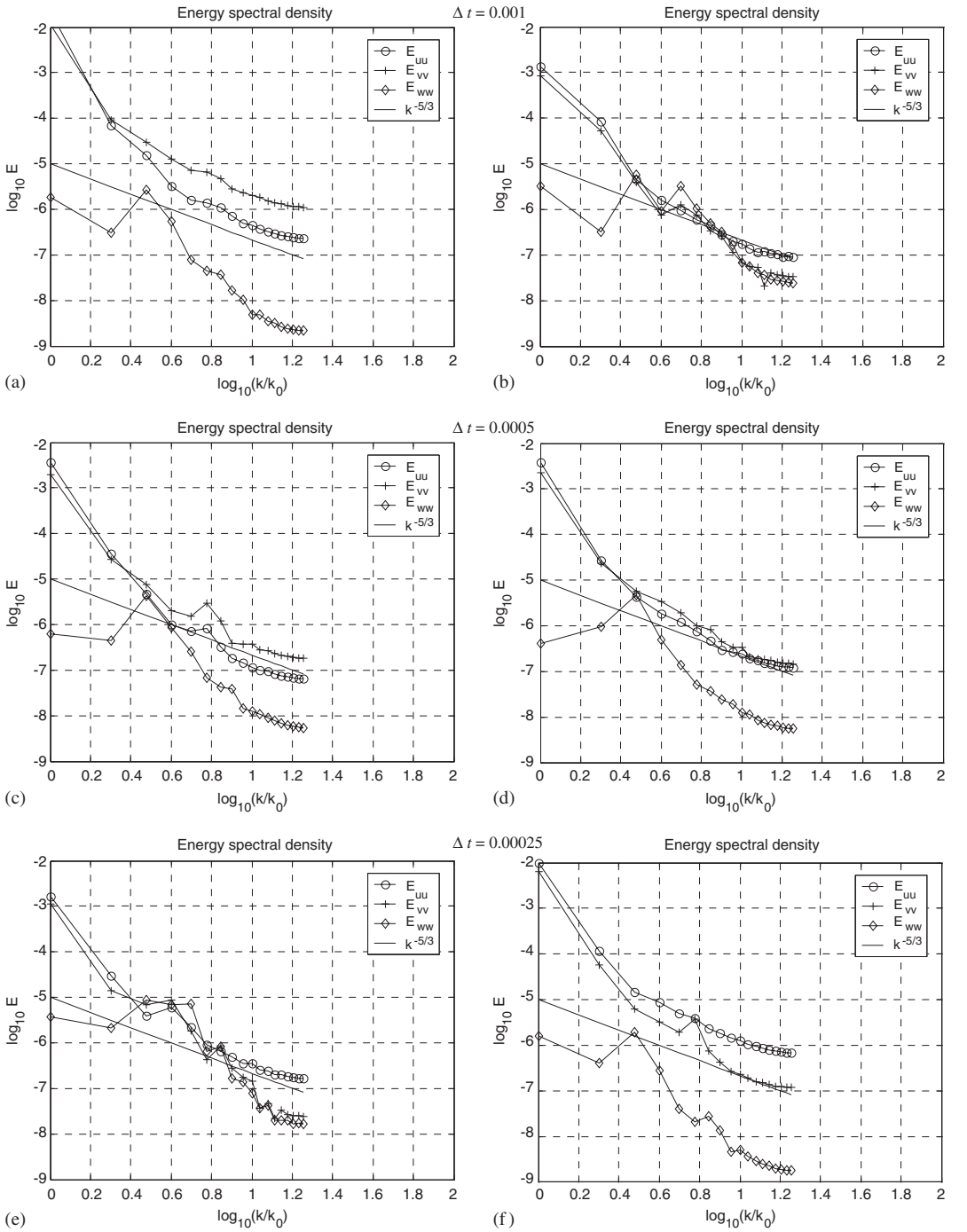

Figure 11. LES of the pulsating channel flow. Stream-wise one-dimensional energy spectra for the velocity components. Intermediate boundary conditions (16) (left column) and (33) (right column).

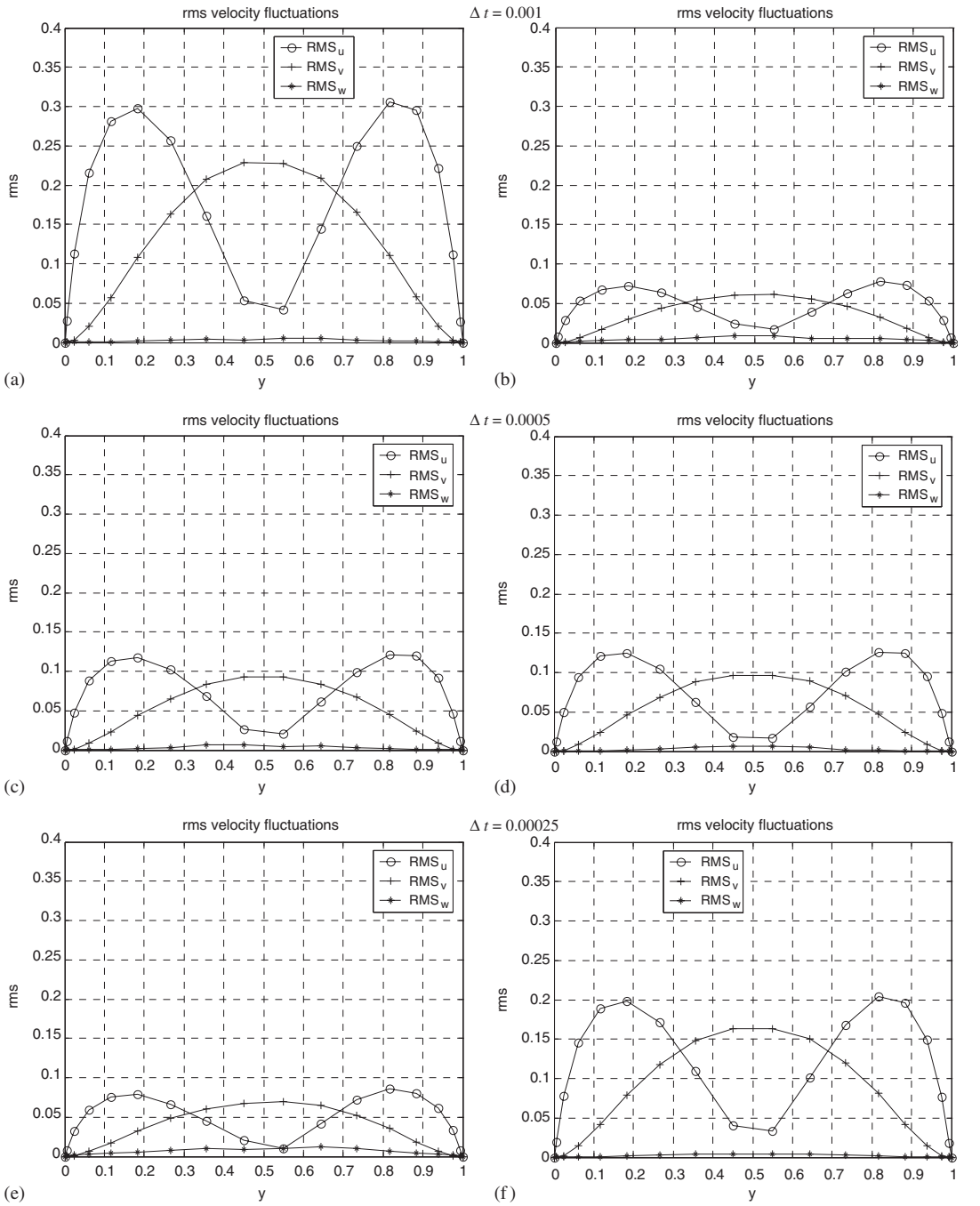

Figure 12. LES of the pulsating channel flow. RMS velocity fluctuations. Intermediate boundary conditions (16) (left column) and (33) (right column).

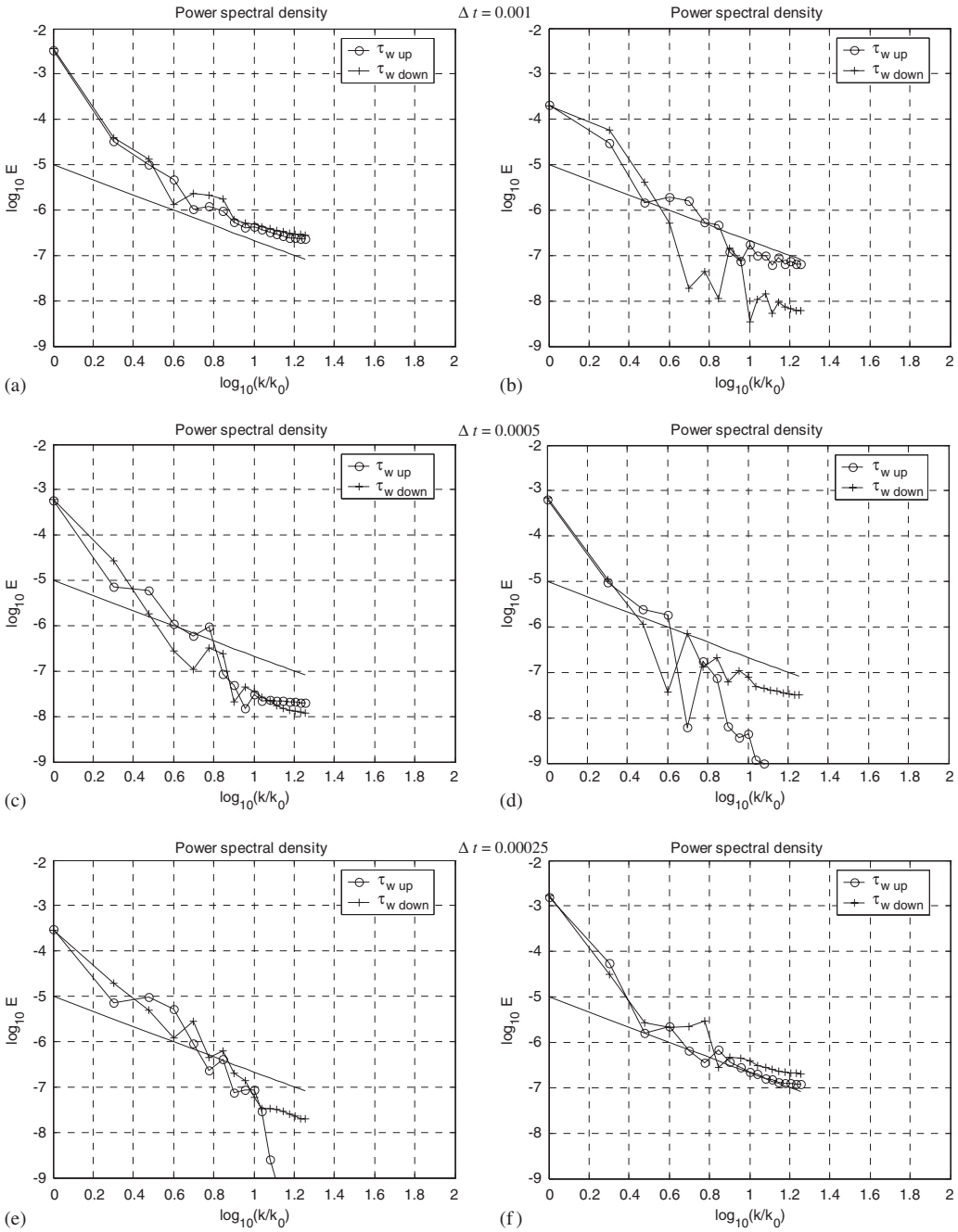

Figure 13. LES of the pulsating channel flow. Stream-wise one-dimensional energy spectra for the stresses on the upper (up) and lower (down) walls. Intermediate boundary conditions (16) (left column) and (33) (right column).

boundary conditions (16) although figure (f) shows a smaller energy level of the span-wise velocity component. Moreover, the columns indicate that the energy levels of u and v velocity components interchange each other at the smallest time-step, see figures (e) and (f).

In Figure 12 are reported the rms velocity fluctuations from which it is always evident the difference in terms of the peaks already analysed in the previous case. Similar to the results obtained for the steady channel, in the left column the peaks magnitude reduces for diminishing time-step while in the right one the peaks magnitude increases (just as observation, (b) and (e) appear quite similar).

Figure 13 illustrates the one-dimensional energy content of the wall stresses (44). The comments are practically the same observed for Figure 9 and again it appears that the results of (f) are superior from those of (e) also taking into account the DNS in Figure 13.

5.2. *Non-periodic channel flow*

The problem that is now illustrated, consists of a flow in a channel with the same geometric parameters of the previous simulations but with an inflow prescribed at $x^{\times} = 0$ and an outflow at $x^{\times} = L_x^{\times}$. Namely, no longer a time-evolving boundary layer but a spatially evolving one is now considered. The aim of this test is to force the vector decomposition to be no longer orthogonal (orthogonality *a priori* existing in the previous biperiodic channel flows) thus allowing the boundary layer mode to interfere with the divergence-free velocity field, see References [10, 11]. The final goal is to show how, depending on the intermediate boundary conditions, the effects propagate also into the interior of the flow.

Spatially evolving turbulent flow simulations require care in prescribing time-dependent inflow conditions since the flow downstream strongly depends on the inlet condition. There are numerous techniques proposed for specifying the time series of inflow profiles, e.g. References [30–32], each one having an appealing characteristic and a computational cost. These techniques focus on the goal of getting a flow field rapidly correlating, just after few boundary layer thickness (from 10 to 20), in a physically meaningful flow field. This should be necessary for both DNS and LES approaches. As a matter of fact, since it is not the aim of the present study to analyse the physical properties of this kind of flow, being instead the goal of this sub-section only of highlighting the differences appearing in the LES results obtained with the boundary conditions (16) and (33), a simple plug inlet is specified.

Furthermore, it is well known that, owing to the strong dumping of disturbances, LES of transitional flow is rather problematic when the static Smagorinsky SGS model is used. Dynamic models or intermittence functions are, therefore, usually considered. Though, in the present simulations, only the results obtained with the Smagorinsky constant fixed to 0.085 are illustrated. In order for the test to be more critical, an 'unphysical' initial condition is specified by repeating the plug-flow along x for generating an inviscid-like initial condition. Therefore, the flow needs to correlate along a wide portion of the channel length and for a long time period. Thus, it is expected that the assignment of accurate intermediate boundary conditions would wholly highlight the discrepancies in the results. The second derivative along x of the auxiliary gradient field is set as outflow condition. Let us observe again that, by adopting these inflow/outflow boundary conditions, decomposition (11) is no longer orthogonal. Since the same processor has been used (i.e. similar data-structure instruction, optimization and round-off), the differences in the flow transition will depend only on the different local truncation error of the intermediate boundary conditions.

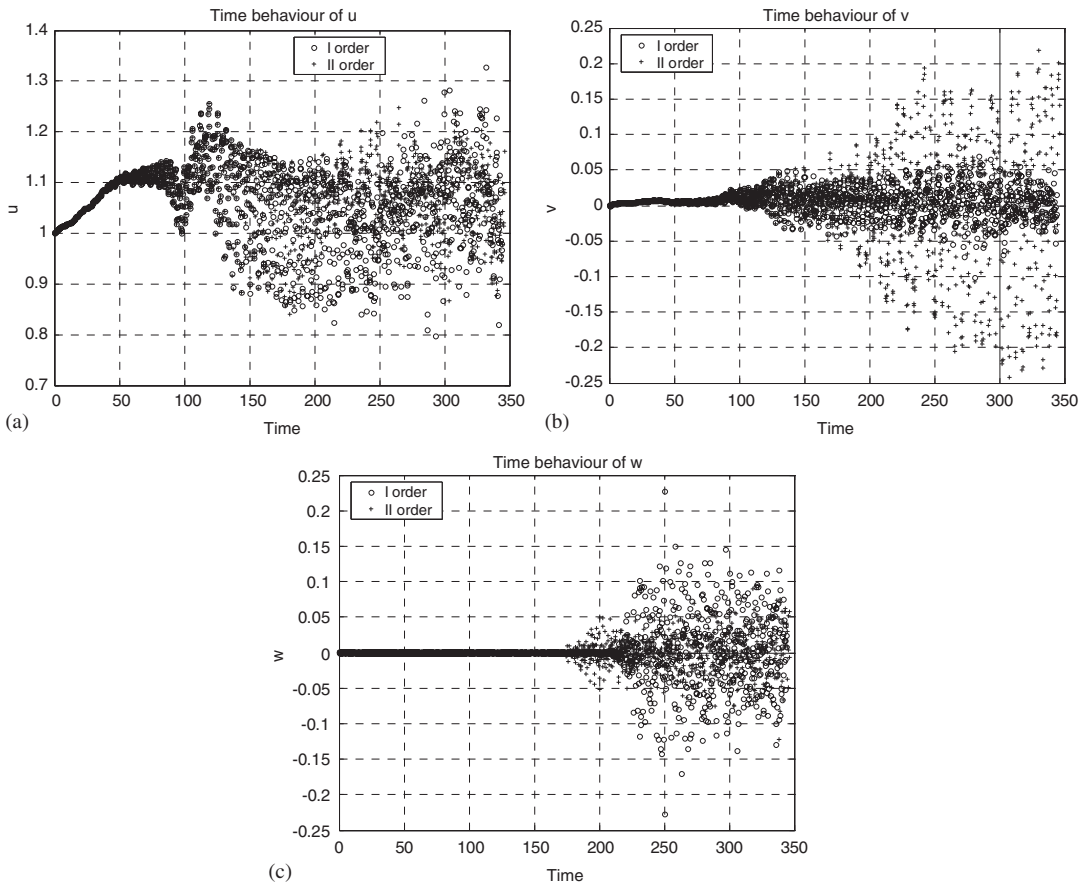

Figure 14. LES of non-periodic channel flow. Time evolution of: (a) stream-wise; (b) vertical; and (c) span-wise velocity components at the centre of the channel for the intermediate boundary conditions (16) and (33).

The Reynolds number, now referred to the inlet velocity, reaches the value 1.18×10^6 at the end of the channel. The adopted LES grid is rather coarse having $35 \times 22 \times 13$ cells thus, one should more properly speak of an 'unresolved' LES. The computational time-step is $\Delta t = 10^{-3}$.

The time-evolution of the three velocity components, in a point located at the centre of the channel, i.e. $(L_x^{\times}/2, L_y^{\times}/2, L_z^{\times}/2)$, is illustrated in Figure 14(a)–(c). They illustrate, after an initial numerical transient, the departure of the behaviours for the solutions obtained with (16) and (33), markedly for the span-wise component. A significant difference is exhibited also for the wall stresses (43), as reported in Figure 15(a),(b). From such evolutions and controlling the RMS, the non-dimensional time for starting the average is chosen as $t_0 = 250$ and the period of integration is $T_{p\_\mathrm{LES}} = 100$. Then, the energy content of the time evolution of the wall stresses is illustrated in Figure 15(c), (d) while the stream-wise one-dimensional is reported in (e), (f). It is evident that the numerical boundary layer affects the velocity

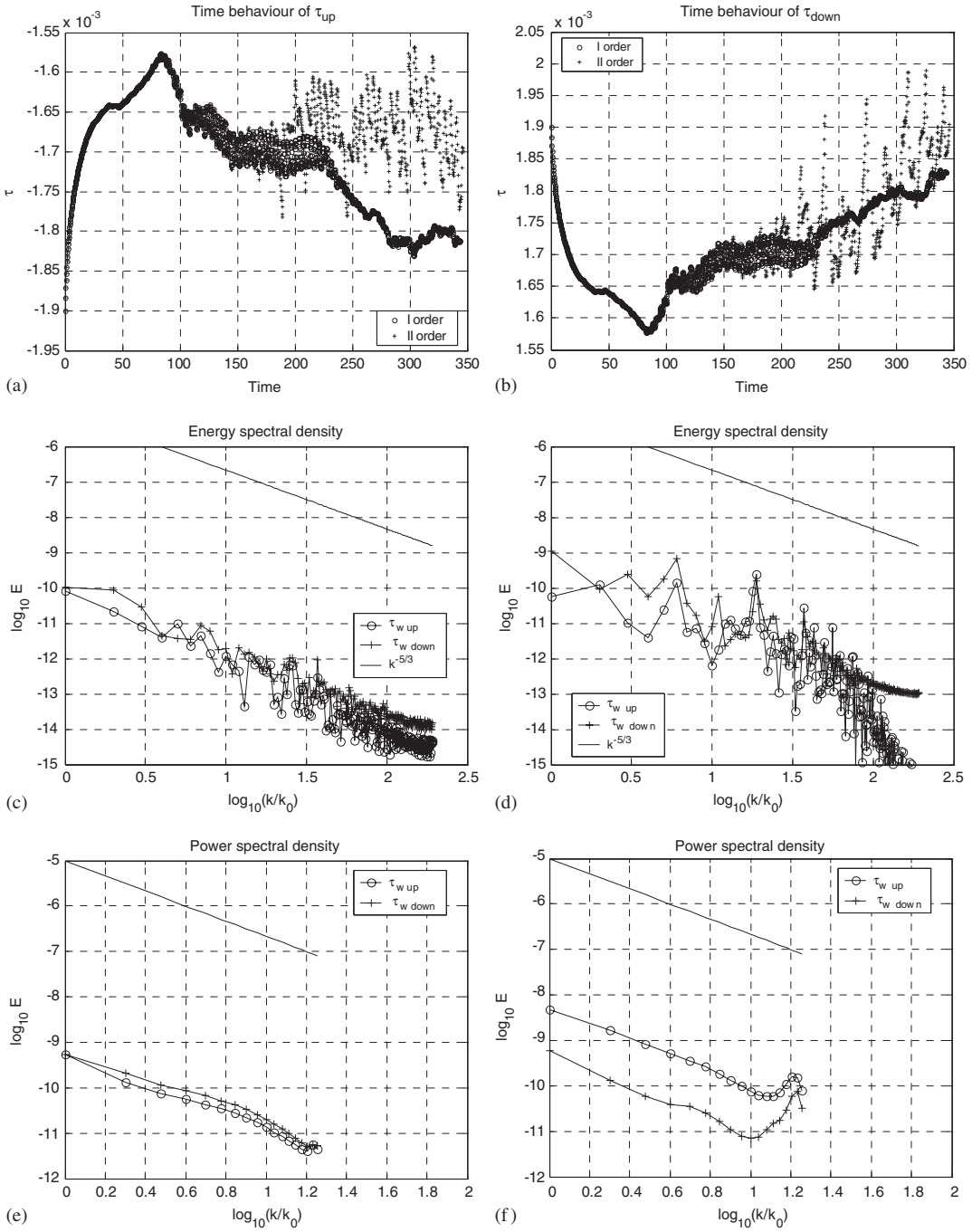

Figure 15. LES of non-periodic channel flow. Time evolution of the stresses on the: (a) upper and; (b) lower walls and the energy spectra of (43); (c), (d) and (44); and (e), (f) for the intermediate boundary conditions (16) (left) and (33) (right).

field in a clear different way: the intermediate boundary condition (16) introduces a higher dissipation than (33). As expected, the discrepancy is much more highlighted in the present non-periodic case.

6. CONCLUSIONS

The development of a new formulation for a better approximation of the intermediate boundary conditions to be used in projection methods for solving incompressible Navier–Stokes equations in both DNS and LES approaches has been illustrated. Particularly, the formulation proposed in Reference [7] has been analysed and improved to a second-order accuracy in time according to References [10, 11]. To the best of the author knowledge, there are no other studies that focused on the congruence between assignment of intermediate boundary conditions and LES formulation. This better approximation is especially expected to improve the simulation of non-homogeneous flows.

The theoretical analysis illustrated how a second-order time-accurate expression for the auxiliary velocity field can be derived, provided that the congruent continuous form of the prediction momentum equation is formulated. In fact, if the discrete character of the auxiliary gradient field is correctly considered and exploited, then the consequent expression takes into account the time evolution of the auxiliary gradient field onto the boundary and the well-known problem of the appearance of the numerical boundary layer. Moreover, such expression is straightforwardly applicable both for DNS and LES approaches since the auxiliary gradient field adapts itself to the specific meaning.

Several DNS and LES simulations, comparing the performances of the first- and second-order intermediate boundary conditions, have been performed. In the specific, the biperiodic steady and pulsating channel flows at $Re_\tau = 70$ have been considered and energy spectra as well as rms of velocity fluctuations are reported. However, such a test is not fully exhaustive of the real accuracy obtainable with the projection methods in LES since the biperiodic channel flow is a very particular test-case wherein the adopted boundary conditions *a priori* guarantee the orthogonality of the HHD. Such feature appears to be much more relevant when the numerical boundary layer mode is not orthogonal to the divergence-free vector space. Therefore, in order for further assessment of the topic to be given, a non-periodic channel flow, for which the vector decomposition is no longer orthogonal, is also tested. Hence, the LES results of the spatially developing boundary layer flow clearly highlighted the discrepancies between boundary conditions (16) and (33).

As a last comment, it is worthwhile observing that the considerations highlighted in this study are particularly relevant when spatial high-order schemes (e.g. spectral or local reconstruction-based) are adopted. Indeed, in such cases, the local truncation error is mainly driven by the time-accuracy that can strongly affect the LES solutions since the filtered variables can be contaminated.

ACKNOWLEDGEMENTS

I have to express my thanks to Dr Vincenzo Botte of the Centro Italiano Ricerche Aerospaziali (CIRA) for helping me during the revision of the paper.

REFERENCES

1. Sagaut P. *Large Eddy Simulation for Incompressible Flows. An Introduction* (2nd edn). Springer: Berlin, 2001.
2. Hodge WVD. *The Theory and Application of Harmonic Integrals*. Cambridge University Press: Cambridge, 1952.
3. Weil H. The method of orthogonal projection in potential theory. *Duke Mathematical Journal* 1940; **7**:411–444.
4. Chorin AJ. Numerical solution of the Navier–Stokes equations. *Mathematics of Computation* 1968; **22**:745–762.
5. Temam R. Sur L'approximation de la Solution des Équations de Navier–Stokes par la Méthode de Pas Fractionnaires (II). *Archives for Rational Mechanics and Analysis* 1969; **33**:377–385.
6. Chorin AJ, Marsden JE. *A Mathematical Introduction to Fluid Mechanics*. Texts in Applied Mathematics, vol. 4. Springer: Berlin, 1990.
7. Kim J, Moin P. Application of a fractional-step method to incompressible Navier–Stokes equations. *Journal of Computational Physics* 1985; **59**:308–323.
8. Brown DL, Cortez R, Minion ML. Accurate projection methods for the incompressible Navier–Stokes equations. *Journal of Computational Physics* 2001; **168**:464–499.
9. Strikwerda JC, Lee YS. The accuracy of the fractional step method. *SIAM Journal on Numerical Analysis* 1999; **37**(1):37–47.
10. Iannelli P, Denaro FM. Analysis of the local truncation error in the pressure-free projection method for the Navier–Stokes equations: a new accurate expression of the boundary conditions. *International Journal for Numerical Methods in Fluids* 2003; **42**:399–437.
11. Denaro FM. On the application of the Helmholtz–Hodge decomposition in projection methods for the numerical solution of the incompressible Navier–Stokes equations with general boundary conditions. *International Journal for Numerical Methods in Fluids* 2003; **43**:43–69.
12. Choi H, Moin P. Effects of the computational time steps on numerical solution of turbulent flows. *Journal of Computational Physics* 1994; **113**:1–4.
13. Pruett CD, Gatski TB, Grosch CE, Thacker WD. The temporally filtered Navier–Stokes equations: properties of the residual stress. *Physics of Fluids* 2003; **15**(8):2127–2140.
14. Chorin AJ. On the convergence of discrete approximations to the Navier–Stokes equations. *Mathematics of Computation* 1969; **23**:341–353.
15. EW, Liu JG. Projection method I: convergence and numerical boundary layers. *SIAM Journal on Numerical Analysis* 1995; **32**(4):1017–1057.
16. EW, Liu JG. Projection method II: Godunov–Ryabenki analysis. *SIAM Journal on Numerical Analysis* 1996; **33**(4):1597–1621.
17. Shen J. On error estimates of the projection methods for the Navier–Stokes equations: second-order schemes. *Mathematics of Computation* 1996; **65**:1039–1065.
18. Wetton BR. Error analysis for Chorin's original projection method with regularization in space and time. *SIAM Journal on Numerical Analysis* 1997; **34**:1683–1697.
19. Guermond JL. Un Résultat de Convergence d'Ordre Deux En Temps Pour L'Approximation Des Équations De Navier–Stokes Par Une Technique De Projection Incrémentale. *Mathematical Modelling and Numerical Analysis* 1999; **33**(1):169–189.
20. Van Kan J. A second order accurate pressure correction scheme for three-dimensional incompressible flow. *SIAM Journal on Scientific Computing* 1986; **21**(7):870–891.
21. Temam R. *Navier–Stokes Equations and Nonlinear Functional Analysis* (2nd edn), vol. 66. SIAM CBMS-NSF: Philadelphia, PA, 1995.
22. Ioveno M, Passoni G, Tordella D. A new large-eddy simulation near-wall treatment. *Physics of Fluids* 2004; **16**:3935–3944.
23. Gustafsson B. The convergence rate for difference approximation to mixed initial boundary value problems. *Mathematics of Computation* 1975; **29**:396–406.
24. LeVeque RJ. Intermediate boundary conditions for LOD, ADI and approximate factorization methods. *ICASE Report No. 85-21*, NASA Langley Research Center, Hampton, VA, 1985.
25. LeVeque RJ. *Finite Volume Methods for Hyperbolic Problems*. Cambridge Press: New York, 2002.
26. Liu M, Ren Y, Zhang H. A class of fully second order accurate projection methods for solving the incompressible Navier–Stokes equations. *Journal of Computational Physics* 2004; **200**:325–346.
27. Iannelli P, Denaro FM, De Stefano G. A deconvolution-based fourth order finite volume method for incompressible flows on non-uniform grids. *International Journal for Numerical Methods in Fluids* 2003; **43**:431–462.
28. Scotti A, Piomelli U. Numerical simulation of pulsating turbulent channel flow. *Physics of Fluids* 2001; **13**:1367–1384.
29. Aprovitola A, Denaro FM. On the application of congruent upwind discretizations for large eddy simulations. *Journal of Computational Physics* 2004; **194**(1):329–343.

30. Lund TS, Wu X, Squires KD. Generation of turbulent inflow data for spatially-developing boundary layer simulations. *Journal of Computational Physics* 1998; **140**:233–258.
31. Li N, Balaras E, Piomelli U. Inflow conditions for large-eddy simulations of mixing layers. *Physics of Fluids* 2000; **12**:935–938.
32. Keating A, Piomelli U, Balaras E, Kaltenbach HJ. *A priori* and *a posteriori* tests of inflow conditions for large-eddy simulation. *Physics of Fluids* 2004; **16**:4697–4712.

